Wide-spread Occurrence and Increasing Trend of Biogenic Aerosol Precursors in the Arctic Ocean Simulated by an Ocean Biogeochemical Model

Moritz Zeising[1], Laurent Oziel[2], Özgur Gürses[1], Judith Hauck[3], Bernd Heinold[4], Svetlana Losa[5], Silke Thoms[6], Manuela van Pinxteren[4], Christoph Völker[7], Sebastian Zeppenfeld[4], and Astrid Bracher[8]

[1]Alfred Wegener Institute Helmholtz Center for Polar and Marine Research
[2]Alfred-Wegener-Institut Helmholtz-Zentrum fur Polar- un Meeresforschung
[3]Alfred Wegener Institute Helmholtz Centre for Polar and Marine Research
[4]Leibniz Institute for Tropospheric Research
[5]Alfred Wegener Inst Polar & Marine Res
[6]Alfred Wegener Institute for Polar and marine Research
[7]Alfred Wegener Institute for Polar and Marine Research
[8]Alfred Wegener Institute

May 5, 2023

Abstract

Biogenic aerosol precursors from phytoplankton production can affect cloud properties, especially in remote regions such as the Arctic Ocean. Reliable estimates on variability and trend of these precursors are required as extensive measurements in the Arctic are still scarce. We present a setup of the coupled ocean biogeochemical model FESOM2.1-REcoM3 where we integrated dissolved carboxylic acid containing polysaccharides (PCHO) and Transparent Exopolymer Particles (TEP) to describe these precursors in the upper ocean. We define PCHO as one part of the excreted organic carbon, which can then aggregate to form larger particles, TEP. Compared to observations, the simulation provides a valid TEP estimate with mean concentrations of 200-400 µg C L-1 on the continental shelves and 10-50 µg C L-1 in the central basins (0-30 m depth range). Further, the simulation for 1990-2019 reveals a significant positive trend of TEP of 0.5-3 µg C L-1 yr-1 during July-September in the Amerasian Basin (+3.5% yr-1), the Canadian Archipelago (+1.2% yr-1) and the Kara Sea (+0.8% yr-1), in contrast to the eastern Fram Strait (-0.4% yr-1), the Barents Sea (-0.3% yr-1), and parts of the Eurasian Basin with a significant decrease of -0.5-2 µg C L-1 yr-1. Our study provides for the first time an integration of TEP formation, aggregation and remineralization processes into a global ocean biogeochemical model. This simulation assembles valuable data on biogenic aerosol precursors, and as such, fills a gap on which Earth System Models can greatly benefit to improve the understanding of aerosol feedbacks within the Arctic climate.

Hosted file

962480_0_art_file_10950472_r41j7x.docx   available   at   https://authorea.com/users/614846/articles/641530-wide-spread-occurrence-and-increasing-trend-of-biogenic-aerosol-precursors-in-the-arctic-ocean-simulated-by-an-ocean-biogeochemical-model

Hosted file

962480_0_supp_10950471_r21j22.docx available at https://authorea.com/users/614846/articles/641530-wide-spread-occurrence-and-increasing-trend-of-biogenic-aerosol-precursors-in-the-arctic-ocean-simulated-by-an-ocean-biogeochemical-model

Wide-spread Occurrence and Increasing Trend of Biogenic Aerosol Precursors in the Arctic Ocean Simulated by an Ocean Biogeochemical Model

M. Zeising[1]*, L. Oziel[1], Ö. Gürses[1], J. Hauck[1], B. Heinold[2], S. N. Losa[1,3], S. Thoms[1], M. van Pinxteren[2], C. Völker[1], S. Zeppenfeld[2], A. Bracher[1,4]

[1]Alfred Wegener Institute Helmholtz Center for Polar and Marine Research, Bremerhaven, Germany.

[2]Leibniz Institute for Tropospheric Research, Leipzig, Germany.

[3]Shirshov Institute of Oceanology, Russian Academy of Sciences, Moscow, Russia.

[4]Institute of Environmental Physics, University of Bremen, Bremen, Germany.

Corresponding author: Moritz Zeising (moritz.zeising@awi.de)

Key Points:

- Occurrence of biogenic aerosol precursors follow phytoplankton blooms in the Arctic Ocean temporally and spatially.

- Highest values of biogenic aerosol precursors are predicted for June-August in the Fram Strait and on the Arctic shelves.

- Simulation shows a split into regions with an increasing and decreasing trend of precursors from 1990 to 2019.

Abstract

Biogenic aerosol precursors from phytoplankton production can affect cloud properties, especially in remote regions such as the Arctic Ocean. Reliable estimates on variability and trend of these precursors are required as extensive measurements in the Arctic are still scarce. We present a setup of the coupled ocean biogeochemical model FESOM2.1-REcoM3 where we integrated dissolved carboxylic acid containing polysaccharides (PCHO) and Transparent Exopolymer Particles (TEP) to describe these precursors in the upper ocean. We define PCHO as one part of the excreted organic carbon, which can then aggregate to form larger particles, TEP. Compared to observations, the simulation provides a valid TEP estimate with mean concentrations of 200-400 µg C L^{-1} on the continental shelves and 10-50 µg C L^{-1} in the central basins (0-30 m depth range). Further, the simulation for 1990-2019 reveals a significant positive trend of TEP of 0.5-3 µg C L^{-1} yr^{-1} during July-September in the Amerasian Basin (+3.5% yr^{-1}), the Canadian Archipelago (+1.2% yr^{-1}) and the Kara Sea (+0.8% yr^{-1}), in contrast to the eastern Fram Strait (-0.4% yr^{-1}), the Barents Sea (-0.3% yr^{-1}), and parts of the Eurasian Basin with a significant decrease of -0.5-2 µg C L^{-1} yr^{-1}. Our study provides for the first time an integration of TEP formation, aggregation and remineralization processes into a global ocean biogeochemical model. This simulation assembles valuable data on biogenic aerosol precursors, and as such, fills a gap on which Earth System Models can greatly benefit to improve the understanding of aerosol feedbacks within the Arctic climate.

Plain Language Summary

Aerosols are tiny particles in the atmosphere, which can affect cloud characteristics. In remote regions as the Arctic Ocean, where land or human impacts are low, local sources of aerosols are important. Small algae in the upper ocean water column can produce precursors of these aerosols, which can then be transferred into the atmosphere. Using an ocean biogeochemical model, these precursors are simulated to occur in summer in higher amounts on the Arctic shelves compared to the central Arctic Ocean basins, which agrees to observations. Furthermore, the simulated precursors exhibit two different trends: an increase in large parts of the Arctic Ocean, and a decrease in the eastern Fram Strait and Barents Sea, analyzing three decades of model output. The results of this study can be useful to simulate more explicitly the impacts of aerosols to the Arctic climate.

1 Introduction

The IPCC expects the polar region, and the Arctic Ocean in particular, to be at the forefront of climate change and profoundly altered in a future world (Pörtner et al. 2019). Those rapid changes are best illustrated by the loss of about 50% of the sea-ice volume during the last decades (Kwok 2018; Serreze & Meiers, 2019 Stroeve & Notz, 2018) and an atmospheric warming up to four times faster than the global averages (Rantenen et al., 2022), the so-called "Arctic Amplification" (Serreze & Barry, 2011). This Arctic Amplification of global warming may be caused by a combination of (positive) feedback processes (Goosse et al., 2018; Pithan & Mauritsen, 2014; Taylor et al., 2022).

Part of these feedback processes are clouds, which have a major role for the Arctic radiation budget (Goosse et al., 2018). The net cloud radiative effect depends on microphysical cloud properties such as the presence of liquid or ice phase (Shupe & Intrieri, 2004). Indeed, measurements suggest that Arctic (liquid-containing) clouds have a net overall surface warming

63 effect throughout the year due to the increase of downwelling longwave radiation, except for a
64 short period in summer (Ebell et al., 2020; Intrieri, 2002). The exact trend and direction of cloud
65 characteristics and their feedback in the Arctic in the context of climate change remains
66 uncertain (Block et al., 2020; Pithan & Mauritsen, 2014; Vihma et al, 2016): On the one hand,
67 the decrease of sea-ice area can lead to increase downwelling longwave radiation in polar winter
68 months via higher low-level cloud cover (positive, i.e. self-reinforcing, feedback); on the other
69 hand, a warmer climate can result in higher liquid content in mixed-phase clouds which leads to
70 higher reflectivity of incoming shortwave radiation in polar summer (Goosse et al., 2018; Pithan
71 & Mauritsen, 2014; Taylor et al., 2022).

72 Especially in remote marine regions, organic aerosol particles out of the upper ocean
73 have been shown to act as cloud condensation nuclei (CCN) or ice nucleating particles (INP)
74 (Hartmann et al., 2020; Irish et al., 2017; Leck & Bigg, 2005; Orellana et al., 2011; Wilson et al.,
75 2015). Further, retreating sea-ice and a warming ocean might result in different temporal
76 occurrence and new local sources of CCN and INP (Schmale et al., 2021; Taylor et al., 2022).
77 Biogenic INP might originate from local features in the open water areas like leads in the sea-ice
78 or ongoing melting cycles (Galgani et al., 2016; Hartmann et al., 2020; Irish et al., 2017;
79 Zeppenfeld et al., 2019). Especially biological active parts of the marginal ice zone and aged
80 melt ponds have been found to contain efficient ice-nucleating substances. Aerosol particles in
81 the Arctic may contain, among many other organic compounds, polysaccharides and
82 proteinaceous material; both two chemical groups are known for their ice nucleating activity
83 (Hawkins & Russell, 2010; Irish et al., 2017; Wilson at el., 2015).

84 Dissolved polysaccharides are combined carbohydrates and belong to the Dissolved
85 Organic Carbon (DOC) pool, which includes carbohydrate, lipid and proteinaceous compounds
86 (Ogawa & Tanoue, 2003). In general, polysaccharides form the major part of the carbohydrate
87 pool in the ocean (Ogawa & Tanoue, 2003; Pakulski & Benner, 1994) and are often carboxylic
88 acid containing (Krembs & Deming, 2008). Phytoplankton produce polysaccharides as anti-
89 freezing agents (Krembs & Deming, 2008), against salinity stress (Steele et al., 2014) or under
90 nutrient stress, when polysaccharides are actively exudated, a process which is referred to as
91 carbon-overconsumption or carbon-overflow (Engel et al., 2004; Engel et al., 2020). Dissolved
92 carboxylic acid containing polysaccharides (PCHO) are defined as dissolved filtered precursors
93 (< 0.2 microns) of Transparent Exopolymer Particles (TEP) and can contribute to the carbon
94 transfer from the dissolved to the particulate organic carbon pool via aggregation of PCHO with
95 other PCHO molecules and aggregation of PCHO with TEP (Alldredge and Crocker, 1995;
96 Passow, 2002). TEP are defined methodologically as particles stainable by Alcian Blue
97 (Alldredge et al., 1993; Engel, 2009; Passow, 2002). From the ocean surface, TEP can be
98 transferred to the atmosphere due to breaking waves and form organic aerosol particles (or sea-
99 spray aerosol particles). Recently, high TEP number concentrations and high TEP mass
100 concentrations were reported in ambient marine aerosol particles, suggesting that gel-like
101 particles can also directly constitute more than half of the particulate organic matter mass (Aller
102 et al., 2017; van Pinxteren et al., 2022). Additionally, TEP have been shown to be a good tracer
103 for other biogenic aerosol formation processes (Park et al., 2019). In this study, we decided to
104 focus on PCHO and TEP formation, because they represent the tracers for biogenic INP that are
105 crucial for cloud formation.

106 Indeed, considering TEP production in Earth System models are expected to greatly
107 improve the representation of clouds and of the Arctic Amplification and the climate projection

108 capacities. However, to the best of our knowledge, TEP formation, aggregation and also
109 remineralization have not been integrated into global ocean biogeochemical models, which also
110 constitute important components of Earth System Models. Cloud formation parametrizations in
111 Earth System Models remain simplistic and do not yet allow to investigate possible feedbacks
112 (Block et al., 2020; Pithan & Mauritsen, 2014).

113 Here, we here aim to fill this gap by integrating, testing and analyzing a TEP
114 parametrization into a "state-of-the-art" ocean biogeochemistry model. We make use of a TEP
115 aggregation model developed by Engel et al. (2004) that was integrated into the third version of
116 the Regulated Ecosystem Model (REcoM3, Gürses et al. 2023). In this study, we focus on the
117 understanding of the seasonal dynamics of TEP production and regional trends in the Arctic
118 Ocean. Because TEP is produced from PCHO during primary production, we firstly assess the
119 performance of this new parametrization by investigating the phytoplankton chlorophyll
120 distribution in the entire Arctic Ocean and examining the bloom phenology in Fram Strait, as an
121 example and data-rich region Then, we present the occurrence patterns and decadal trends of
122 TEP throughout the Arctic Ocean and put them into perspective of the global ocean.

2 Materials and Methods

124 We first introduce the specific ocean biogeochemical model FESOM-REcoM used
125 (section 2.1), before detailing the model implementation of DOC, PCHO and TEP (section 2.2),
126 the specifications of the model simulation (section 2.3), the processing of model results (section
127 2.4), and presenting the evaluation data sets from remote sensing and *in situ* measurements
128 (section 2.5).

2.1 Ocean circulation and biogeochemical model

130 We used the coupled setup of the biogeochemical Regulated Ecosystem Model version 3
131 (REcoM3) and the general circulation and sea-ice Finite VolumE Sea-ice Ocean Model version
132 2.1 (FESOM2.1). FESOM is an unstructured-mesh ocean circulation model which allows high
133 spatial resolution in dynamically active regions, while including the remainder of the global
134 ocean at a coarse resolution (Wang et al., 2014). FESOM applies a finite-volume discretization
135 instead of finite-elements previously used, optimizing computational costs and enabling a
136 straight-forward flux definition (Danilov et al., 2017; Koldunov et al., 2019).

137 REcoM3 represents the ocean biogeochemistry and ecosystem, and describes the carbon
138 cycle, nutrients (N, Si, Fe), two phytoplankton functional types (namely diatoms and
139 nanophytoplankton), two zooplankton types (small zooplankton, polar macrozooplankton),
140 dissolved as well as particulate organic matter, and detritus. Gravitational sinking of particles
141 through the water column is simulated with depth-dependent sinking speed, and accumulation in
142 the benthos is represented by one benthic layer. The model allows for variable phytoplankton
143 stoichiometry (Hauck et al., 2013; Schourup-Kristensen et al., 2014). A first version of REcoM
144 was presented in Schartau et al. (2007), a second version (REcoM2) was developed by Hauck et
145 al. (2013) and Schourup-Kristensen et al. (2014), while REcoM3 was extended to include two
146 zooplankton and detritus classes developed by Karakuş et al. (2021). Gürses et al. (2023) present
147 a detailed description and assessment of the REcoM3 performance on the global scale. As a
148 result of model development to REcoM2 and 3, the organic carbon pools were adapted to take
149 into account the two phytoplankton, two zooplankton, and two detritus classes. For this study, we
150 specified the cycle of organic carbon through the dissolved, particular and intracellular carbon

151 pools by adding the process description for dissolved carboxylic acidic containing

152 polysaccharides (PCHO) and Transparent Exopolymer Particles (TEP), following Engel et al.

153 (2004) and Schartau et al. (2007). REcoM3 now includes 30 different biogeochemical tracers

154 (c.f. Tab. A1 in Gürses et al., 2023).

155   2.2 Model implementation of dissolved organic carbon, polysaccharides and transparent

156   exopolymer particles

157   Engel et al. (2004) and Schartau et al. (2007) developed generalized equations and

158 parametrization for the excretion and aggregation of organic carbon particles. The quantitative

159 description of these processes was obtained by a mesocosm experiment of Engel et al. (2004)

160 and consecutively integrated in the first version of the Regulated Ecosystem Model (Schartau et

161 al., 2007). The PCHO and TEP pool were omitted in recent model releases but re-integrated in

162 this study. In a first step, organic carbon is exudated by phytoplankton as two different dissolved,

163 labile compounds: as PCHO and as residual DOC (considered consisting of labile organic

164 compounds, but the chemical composition is not specified in greater detail). In a second step,

165 multiple PCHO molecules may form aggregates, or adhere to already existing TEP particles.

166   DOC sources are now represented with excretion of intracellular carbon by both

167 phytoplankton and both zooplankton classes, and detrital carbon degradation of both detritus

168 classes. The remineralization to Dissolved Inorganic Carbon (DIC) is the only sink for DOC. The

169 simulated source minus sinks term results as follows (see list of variables, parameters below):

$$S(DOC) = \underbrace{(1 - f_{PCHO}) \cdot \varepsilon_{phy}^C \cdot f_{phy}^{lim} \cdot C_{phy}}_{\text{excretion by small phytoplankton}} + \underbrace{(1 - f_{PCHO}) \cdot \varepsilon_{dia}^C \cdot f_{dia}^{lim} \cdot C_{dia}}_{\text{excretion by diatoms}}$$

$$+ \underbrace{\varepsilon_{zoo1}^C \cdot C_{zoo1}}_{\text{excretion by zooplankton}} + \underbrace{\varepsilon_{zoo2}^C \cdot C_{zoo2}}_{\text{excretion by macrozoo.}} + \underbrace{\rho_{POC} \cdot f_T \cdot C_{det1} + \rho_{POC} \cdot f_T \cdot C_{det2}}_{\text{remineralization of detritus}}$$

$$- \underbrace{\rho_{DOC} \cdot f_T \cdot C_{DOC}}_{\text{remineralization to DIC}}$$

170   (1)

171   The limiter functions f_{phy}^{lim} and f_{dia}^{lim} regulate the phytoplankton metabolic processes via a

172 non-linear function based on the intracellular nitrogen to carbon ratios (N:C ratio) following

173 Geider et al. (1998) and modified for REcoM in Schourup-Kristensen et al. (2014). The limiter

174 function is zero for N:C ratios above the set value of N:C = 21.2:106 = 0.2. No nitrogen uptake

175 and no carbon excretion take place. When the N:C ratio becomes lower, the limiter function

176 increases, hence, both nitrogen uptake and carbon excretion of phytoplankton start. When the

177 current N:C ratio is lower than the Redfield ratio (N:C = 16:106 = 0.151), the limiter function is

178 one, not limiting uptake nor excretion (c.f. Section A3.6 in Gürses et al, 2023; Section A6.1 in

179 Schourup-Kristensen et al., 2014).

180   We implemented the source and sink terms for PCHO and TEP into the current REcoM

181 version 3 as follows: A fraction of the excreted organic carbon by small phytoplankton and

182 diatoms builds up the PCHO pool, the aggregation of PCHO with other PCHO or with already

183 existing TEP decrease the PCHO pool. These aggregation processes are described as cluster-

184 cluster aggregation via Smoluchowski equations (Engel et al., 2004 and references therein) and

185 depend on the concentration of PCHO and TEP, on the stickiness of the substrates, and on the

186 collision kernels specific for PCHO-PCHO and PCHO-TEP interaction (c.f. Box 1 in Engel et

187 al., 2004). The collision kernels describe the probability of encounter of molecules. The TEP
188 pool is increased by aggregation products of PCHO-PCHO and PCHO-TEP and diminished by
189 remineralization to DIC.

$$S(PCHO) = \underbrace{f_{PCHO} \cdot \varepsilon_{phy}^C \cdot f_{phy}^{lim} \cdot C_{phy}}_{\text{excretion by small phytoplankton}} + \underbrace{f_{PCHO} \cdot \varepsilon_{dia}^C \cdot f_{dia}^{lim} \cdot C_{dia}}_{\text{excretion by diatoms}}$$

$$- \underbrace{\alpha_{PCHO} \cdot \beta_{PCHO} \cdot C_{PCHO} \cdot C_{PCHO}}_{\text{aggregation of PCHO with PCHO}} \qquad (2)$$

$$- \underbrace{\alpha_{TEP} \cdot \beta_{TEP} \cdot C_{PCHO} \cdot C_{TEP}}_{\text{aggregation of PCHO with TEP}}$$

190

$$S(TEP) = \underbrace{\alpha_{PCHO} \cdot \beta_{PCHO} \cdot C_{PCHO} \cdot C_{PCHO}}_{\text{aggregation of PCHO with PCHO}}$$

$$+ \underbrace{\alpha_{TEP} \cdot \beta_{TEP} \cdot C_{PCHO} \cdot C_{TEP}}_{\text{aggregation of PCHO with TEP}} \qquad (3)$$

$$- \underbrace{\rho_{TEP} \cdot f_T \cdot C_{TEP}}_{\text{remineralization to DIC}}$$

191

192 where the descriptions of state variables, parameters and functions are listed in Table 1.

193 **Table 1.** List of state variables, parameters and functions used in the model implementation of
194 Dissolved Organic Carbon (DOC), dissolved carboxylic acid containing polysaccharides
195 (PCHO) and Transparent Exopolymer Particles (TEP).

State variables	Description	Value	Unit
C_{phy}	carbon concentration of small phytoplankton		[mmol C m^{-3}]
C_{dia}	carbon concentration of diatoms		[mmol C m^{-3}]
C_{zoo1}	carbon concentration of zooplankton		[mmol C m^{-3}]
C_{zoo2}	carbon concentration of polar macrozooplankton		[mmol C m^{-3}]
C_{det1}	carbon concentration of detritus class 1		[mmol C m^{-3}]
C_{det2}	carbon concentration of detritus class 2		[mmol C m^{-3}]
C_{DOC}	carbon concentration of DOC		[mmol C m^{-3}]
C_{PCHO}	carbon concentration of PCHO		[mmol C m^{-3}]
C_{TEP}	carbon concentration of TEP		[mmol C m^{-3}]
N_{phy}	nitrogen concentration of small phytoplankton		[mmol N m^{-3}]
N_{dia}	nitrogen concentration of small phytoplankton		[mmol N m^{-3}]
N_{det1}	nitrogen concentration of detritus class 1		[mmol N m^{-3}]
N_{det2}	nitrogen concentration of detritus class 2		[mmol N m^{-3}]
Parameters			
f_{PCHO}	fraction of PCHO of excreted organic carbon	0.634	
α_{PCHO}	stickiness for PCHO-PCHO	0.00087	
α_{TEP}	stickiness for PCHO-TEP	0.4	
β_{PCHO}	C-based aggregation kernel for PCHO-PCHO	0.86	[m^3 mmol C^{-1} d^{-1}]
β_{TEP}	C-based aggregation kernel for PCHO-TEP	0.064	[m^3 mmol C^{-1} d^{-1}]
ε_{phy}^{C}	excretion rate of organic C by small phytoplankton	0.1	[d^{-1}]
ε_{dia}^{C}	excretion rate of organic C by diatoms	0.1	[d^{-1}]
ε_{zoo1}^{C}	excretion rate of organic C by zooplankton	0.15	[d^{-1}]
ε_{zoo2}^{C}	excretion rate of organic C by polar macrozooplankton	0.02	[d^{-1}]
ρ_{DetC}	remineralization constant of detritus	0.15	[d^{-1}]
ρ_{DOC}	remineralization constant of DOC	0.1	[d^{-1}]
ρ_{TEP}	remineralization constant of TEP	0.1	[d^{-1}]
ϕ_{PP}	N-based maximum aggregation loss parameter for plankton	0.015	[m^3 mmol N^{-1} d^{-1}]
ϕ_{PD}	N-based maximum aggregation loss parameter for detritus	0.165	[m^3 mmol N^{-1} d^{-1}]
k_{TEP}	half-saturation const. of TEP controlled particle stickiness for aggregation of phytoplankton cells	45.0	[mmol C m^{-3}]
Functions			
f_{phy}^{lim}	limiter function for the small phytoplankton carbon excretion rate		
f_{dia}^{lim}	limiter function for the diatom carbon excretion rate		
f_T	temperature-depending Arrhenius function		

196

197   The aggregation of particles determines the amount of diatom and small phytoplankton
198 carbon, nitrogen, and silicate transferred to the corresponding detritus pools. The aggregation
199 rate *g* was calculated based on REcoM2 (see eq. 16 in SI to Hauck et al., 2013) combined with a
200 coagulation kernel, which describes the particle stickiness depending on TEP concentration (see

201 eq. B13 in Schartau et al., 2007). High TEP concentrations (C_{TEP}) increase the particle stickiness
202 and, thus, the aggregation rate g.

$$g = \quad (\phi_{PP} \cdot N_{phy} + \phi_{PP} \cdot N_{dia} + \phi_{PD} \cdot N_{det1} + \phi_{PD} \cdot N_{det2}) \qquad (4)$$

203 $$\cdot \frac{C_{TEP}}{k_{TEP} + C_{TEP}}$$

204 where state variables and parameters are described in Table 1.

205   2.3 Specific model setup and simulation

206   For this study, we run FESOM2.1-REcoM3 with 4.5 km resolution in the Arctic Ocean
207 (north of 60°N), with the so-called fARC mesh (https://gitlab.awi.de/fesom/farc) (Wang et al.,
208 2018, Wekerle et al., 2017; Schourup-Kristensen et al., 2018). After the evaluation of the model
209 skills to represent primary production dynamics, we turned off the photo-damage parametrization
210 (Alvarez et al., 2019) and turned on the aeolian and riverine nitrogen input, and benthic
211 denitrification included in REcoM3. We follow the parametrization of model processes as
212 presented in Gürses et al. (2023). We started the ocean simulation from initial temperature and
213 salinity fields from the Polar Science Center Hydrographic Climatology (Steele et al., 2001) and
214 the biogeochemical simulation from initial fields of Dissolved Inorganic Nitrogen (DIN) and
215 Dissolved Silic Acid (DSi) concentration from the World Ocean Atlas climatology (Garcia et al.,
216 2019a, 2019b), and Dissolved Inorganic Carbon (DIC) as well as alkalinity from Global Ocean
217 Data Analysis Project (GLODAP) version 2 (Lauvset et al., 2016). Riverine inputs of inorganic
218 and organic carbon and nitrogen are derived from Terhaar et al. (2021).

219   Simulations were carried out for the period 1958-2019, i.e., a total of 61 years, with
220 atmospheric forcing from the atmospheric reanalysis data sets of JRA55-do v.1.4.0 (Tsujino et
221 al., 2018). We considered the period 1958-1990 as spin-up, which allows the biological
222 processes in the surface ocean to reach quasi-equilibrium. The period of 1990-2019 was
223 analyzed. We obtained monthly output for all years, and in addition daily output for April to
224 September of 2017 for comparison to *in situ* observations from the ship-based "Physical
225 feedbacks of Arctic Boundary Layer Sea ice, Cloud And Aerosol (PASCAL)" campaign PS106
226 on RV Polarstern. A campaign overview is presented in Macke & Flores, 2018 and Wendisch et
227 al., 2019.

228   2.4 Data processing

229   We calculated the volume-weighted mean concentration $\bar{c}_{vw}$ for each grid cell over the
230 depth range as:

231 $$\bar{c}_{vw} = \frac{\sum_i A * d_i * c_i}{V_{tot}}$$

232 $$V_{tot} = A * \sum_i d_i = A * d$$

233 with area A, thickness d_i of layer with index i, and concentration c_i corresponding to that layer.

234   An overall spatial mean and 0.25, 0.5, and 0.75 quantile concentrations were computed
235 using these monthly volume-weighted mean data. A standard deviation was calculated from the
236 volume-weighted mean over the monthly time steps. Trends were computed as linear least-
237 square regressions based on data averaged for the months April-June and July-September over

238 the period 1990-2019. For regional trends, these were computed based on the corresponding
239 regional mean and their percentaged increases were predicted from the linear regression results
240 comparing the years 1990 to 2019. For comparison to observational data sets, we calculated a
241 volume-weighted mean concentration of simulated TEP concentration over the same depth range
242 as stated for observational data sets. The standard deviation was calculated over the grid points
243 inside the area of concern and over the specific month corresponding to the observation data
244 used.

245   Analysis was carried out for the Arctic Ocean and put into global perspective. Boundaries
246 for the Arctic Ocean Basins and Seas (Fig. 1) were set according to Nöthig et al. (2020) and
247 Randelhoff et al. (2020). As Supplementary Information, we calculated volume-weighted mean
248 TEP and PCHO concentrations binned for Longhurst provinces (Longhurst, 2006).

249   2.5 Remote-sensing and *in situ* data sets for model validation

250   For validation of our simulation, we used the Arctic Copernicus Marine Environment
251 Monitoring Service level 4 monthly reprocessed Ocean Color product (Product ID:
252 OCEANCOLOUR_ARC_BGC_L4_MY_009_124) with resolution of 4 km for Total
253 Chlorophyll *a* (TChla) – CMEMS, in the following – (Copernicus Marine Service & PML,
254 2022). Matching the last two decades of our simulation, CMEMS data of 2000-2019 was
255 downloaded and processed by averaging to a summer mean concentration for TChla and its error
256 for the months May-September. Both CMEMS and FESOM-REcoM data were interpolated to a
257 regular grid of 0.2 degrees for comparison. As Supplementary Information, we used the Arctic
258 Ocean Total Chlorophyll *a* product based on "AOreg.emp" from Lewis et al. (2020), constituting
259 of the years 2003-2019, of which the Modis/Aqua TChla only was processed.

260   The simulated PCHO represents the dissolved carboxylic acid containing carbohydrates,
261 which are reported to form the major part of dissolved carbohydrates in the ocean (Krembs &
262 Deming, 2008), complemented by a small fraction of dissolved free carbohydrates (various
263 monosaccharides). Since no observations on PCHO are available, we chose to compare
264 simulated PCHO to *in situ* measured dissolved combined carbohydrates (DCCHO)
265 concentration. These were derived from field bulk water samples collected at 1 m depth during
266 the 2017 PASCAL campaign on RV Polarstern following the protocol of Zeppenfeld et al.
267 (2020) using high-performance anion exchange chromatography coupled with pulsed
268 amperometric detection (HPAEC-PAD). For the validation, field sample results were
269 differentiated into three groups: (a) ice-free ocean, (b) MIZ (MIZ), and (c) leads/polynyas within
270 the ice pack. For the model validation, we only considered the means and standard deviations of
271 DCCHO concentration from each of the three groups. This data set is as available at Zeppenfeld
272 et al. (2023).

273   TEP can be determined in water samples observationally by microscopy of abundances of
274 particles [# L^{-1}] or determination of particle surface area [cm^2 L^{-1}] (Engel et al., 2020, Engel et
275 al., 2009), or colorimetrically by staining with Alcian Blue solution resulting in Xanthan gum
276 equivalents [µg Xeq L^{-1}] (Engel et al., 2009, Alldredge et al., 1993). As these methods are not
277 fully comparable to one another, we prioritized colorimetric determined TEP. Data on *in situ*
278 TEP concentration were converted to [µg C L^{-1}], as REcoM biogeochemical processes were
279 described in units of carbon (TEP-C). Namely, we used data sets of Engel et al. (2020), von
280 Jackowski et al. (2020), Yamada et al. (2015), and Wurl et al. (2011). Further, TEP concentration

281 of Yamada et al. (2015) were converted from Xanthan gum equivalents [µg Xeq L^{-1}] to carbon
282 [µg C L^{-1}] by a factor of 0.05*12.01 following Engel et al. (2020).
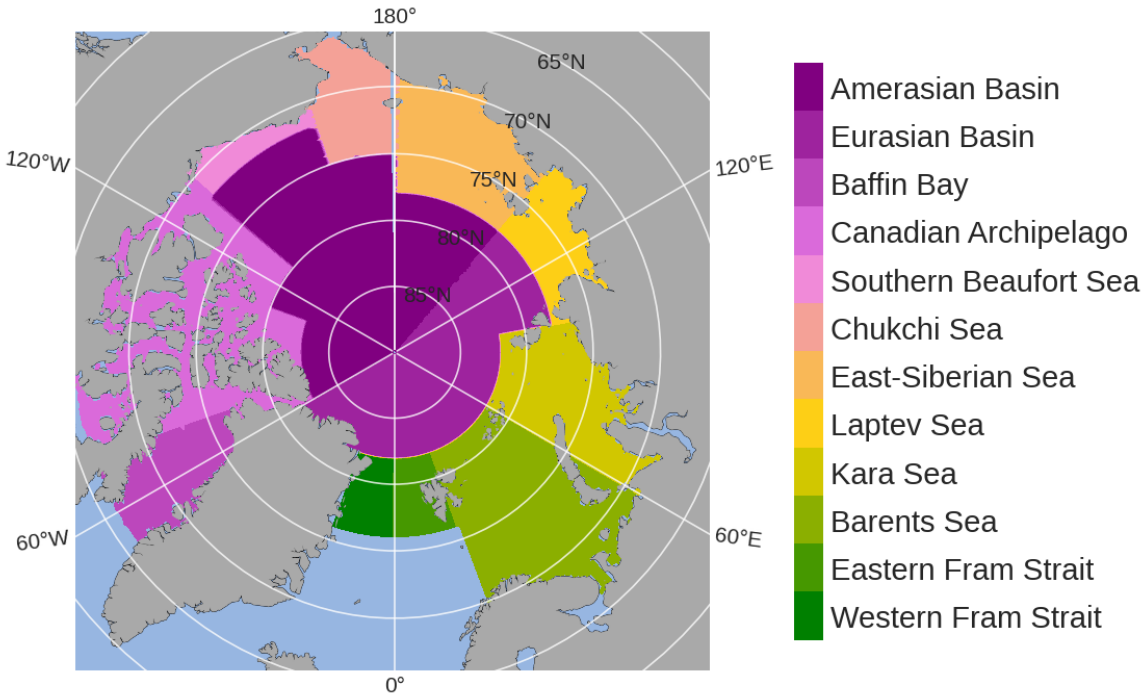
283

284
285 **Figure 1**. Map of Arctic Ocean basins and seas for evaluation of biogeochemical properties in
286 this study, based on Nöthig et al. (2020) and Randelhoff et al. (2020).

287

3 Results and Discussion

289   Within this study, we simulate tracers for biogenic aerosol precursors by implementing
290 the formation and degradation processes of PCHO and TEP into FESOM2-REcoM3 (Gürses et
291 al., 2023). While this is a global model, its specific setup can be optimized in its parametrizations
292 for the Arctic Ocean, for which already in previous setups, the Arctic biogeochemistry was
293 simulated successfully with regard to primary production, light and nutrient availability (Oziel et
294 al., 2022; Schourup-Kristensen et al., 2021; Schourup-Kristensen et al., 2018). In the following
295 we present for the Arctic Ocean our new setup's predictions of phytoplankton distribution in
296 terms of TChla and Particulate Organic Carbon (POC) concentrations (Section 3.1) and the link
297 of phytoplankton phenology to the predicted PCHO (Section 3.2). Section 3.3 focuses on its link
298 to TEP and Section 3.4 on the derived regional trends over the last three decades. Finally, we
299 discuss in Section 3.5 the perspectives of the new developed FESOM-REcoM setup for global
300 applications. In all sections FESOM-REcoM predictions are evaluated by comparisons with *in
301 situ* and remote sensing observations, and by assessment of spatial and seasonal patterns.

302   3.1 Phytoplankton distribution in the Arctic Ocean

303   The Arctic setup of FESOM-REcoM simulates the phytoplankton seasonal cycle, where
304 phytoplankton depends on nutrient and light availability and is controlled by zooplankton

305   grazing, aggregation and degradation losses, which we evaluate with Arctic remote sensing and
306   *in situ* observations.

307   Figure 2 shows the phytoplankton biomass in the Arctic surface ocean in terms of TChla
308   from our FESOM-REcoM simulations and compares it to the CMEMS Arctic satellite re-
309   analysis product as average over the years 2000-2019 (as a mean model state) for the months
310   when also satellite data can be obtained. FESOM-REcoM predicts highest TChla of up to
311   6 mg m^{-3} along the Siberian coast and on other shelf seas between 0.5-3 mg m^{-3}(Fig. 2A). In the
312   Fram Strait, TChla predictions range from 1 to 3 mg m^{-3} with highest values in its central part,
313   while in the central basins of the Arctic Ocean, TChla is low, with values of less than 0.2 to
314   0.8 mg m^{-3}. The CMEMS Arctic reanalysis remote-sensing TChla product shows no coverage of
315   the central Arctic Ocean due to the satellite sensors configuration not enabling observations at
316   these high latitudes (Fig. 2B). In the Barents, Kara, and Laptev Sea, TChla ranges from 0.5-
317   5 mg m^{-3}, with peaks of up to 15 mg m^{-3} close to the coastline. In the East Siberian, Chukchi, and
318   Beaufort Sea, the concentration of TChla is lower, ranging from 0.1-1 mg m^{-3}, also with very
319   high values close to the coast. The error of TChla provided with the CMEMS TChla product is
320   mostly lower than 0.5 mg m^{-3}, however along the coastline, the error increases to more than
321   2 mg m^{-3} (Fig. 2D). The FESOM-REcoM TChla range agrees well with CMEMS TChla, except
322   for the inner shelf areas (Fig. 2C): In the Barents, Kara, and Laptev Sea and close to the
323   Canadian coast FESOM-REcoM is much lower (see above). Whereas in the Chukchi and
324   Beaufort Sea and western Fram Strait, FESOM-REcoM predicts higher TChla than CMEMS.
325   One explanation for the observed difference may be that CMEMS average values sample far less
326   days then are simulated by FESOM-REcoM. Schourup-Kristensen et al. (2018) explain lower
327   TChla in the simulation by full spatial and temporal coverage whereas only open-water
328   productive regions are accessible from remote sensing measurements. Additionally, CMEMS is
329   error-prone on large parts of the Siberian shelves, most likely due to the very high colored
330   dissolved organic matter and total suspended matter concentrations not accounted for in the
331   retrieval and resulting in a strong overestimation of TChla (Heim et al., 2014; Schourup-
332   Kristensen et al., 2018). Also, our model results show realistically the high DOC values along
333   the coasts (data not shown). In the Chukchi and Beaufort Sea, the simulated TChla concentration
334   itself (and the difference of FESOM-REcoM to CMEMS) is low in total values (less than
335   1.5 mg m^{-3}). Other observations from *in situ* observation data and other satellite-derived products
336   draw a diverse picture in these seas with massive under-ice blooms in the Chukchi Sea with high
337   TChla values of up to 30 mg m^{-3} (Arrigo et al. 2014), and low (0.02-0.25 mg m^{-3}) TChla
338   concentration in the northern Chukchi and Beaufort Sea (Jung et al., 2022; Park et al. 2019).

339   Comparing FESOM-REcoM to the Arctic TChla product presented in Lewis et al. (2020),
340   the range of agreement is similar as to the CMEMS product, but the spatial patterns are very
341   different (Fig. S1 in Supplementary): This satellite product shows even lower TChla
342   concentration in large parts of the Arctic, but agrees better to our predictions in the southern
343   Barents Sea and Laptev Sea shelf break where TChla is still a bit higher with reaching maximum
344   values of 7 mg m^{-3}. The authors derive TChla estimates by differentiating retrieval parameters
345   regionally, as developed by Lewis and Arrigo (2020). This leads to a good fit to *in situ*
346   measurements but produces abrupt changes in TChla estimates across region boundaries. The
347   choice of methods (CMEMS compared to Lewis et al., 2020) profoundly impacts the remote
348   sensing products. In this study, we decided to give priority to the CMEMS Arctic TChla product
349   as it is more consistent across the whole Arctic Ocean, despite overestimation on the inner
350   shelves.

351   Since satellite products have quite large errors (25-150%) and standard deviation (Fig. S1
352 in Supplementary) in the Arctic Ocean, we also compared our FESOM-REcoM simulations to *in*
353 *situ* observations. A valuable dataset for our model evaluation is the long-term compilation of *in*
354 *situ* observation data of TChla of Fram Strait and adjacent Arctic seas covering mainly the
355 summer months May to September 1991 to 2015, presented in Nöthig et al. (2020). Following
356 this study, we split the results of our predictions into box plots for different Arctic regions (Fig.
357 3), summarizing the summer months May to September of 2000-2019 (to match to the model
358 time frame presented in Fig. 2 consistently) and evaluated for the upper 100 m depth-integrated
359 data. TChla predictions range between 0.01-69.2 mg m^{-2} regarding 1st to 3rd quartile. Values are
360 highest in the eastern Fram Strait with median values around 40.4 mg m^{-2}. In the western Fram
361 Strait and in the Siberian seas, TChla median ranges from 24.5-32.9 mg m^{-2}. In the Eurasian and
362 Amerasian Basin, median of TChla concentration is close to zero mg m^{-2} with 1st and 3rd quartile
363 containing 0.002-14.2 mg m^{-2}. FESOM-REcoM produces some outliers with up to 350 mg m^{-2} in
364 the eastern Fram Strait or Chukchi Sea.

365   Our TChla predictions compare well to the results from Nöthig et al. (2020) but also to
366 other observations: In eastern Fram Strait, *in situ* measurements of Nöthig et al. (2020) result in
367 integrated median values of 44 mg m^{-2} (0-100 m), and in Barents Sea of 42 mg m^{-2} which fit our
368 model results of 40.4 and 33.8 mg m^{-2}, correspondingly (Fig. 3A). Our results are also in line
369 with two-year round mooring observations at the long-term ecological research observatory
370 HAUSGARTEN in the eastern Fram Strait with simulated TChla concentration reaching up to
371 5 mg m^{-3} in the upper 30 m compared to 7 mg m^{-3} in measurements (von Appen et al., 2021). In
372 the marginal ice zone (MIZ), especially in the area of Fram Strait, phytoplankton growth is
373 expected to be highest, as the sea-ice breaks up, light availability is increased and the water
374 column is stratified (Cherkasheva et al., 2014; Nöthig et al., 2020). Likewise in the western part
375 of Fram Strait and in the Siberian seas, the lower amount of TChla from our simulations matches
376 *in situ* data for these regions spanning from 13-26 mg m^{-2} (Nöthig et al, 2020; Piontek et al.,
377 2021). Integrated TChla is even lower in the Arctic Ocean basins in both simulation (median
378 0.01 mg m^{-2}) and measurements (7-8 mg m^{-2}). A likely explanation for the higher computed
379 median TChla in several regions and higher variability in comparison to Nöthig et al. (2020)
380 might be the consideration of 6-62k data points in the region subsets (Figure 1) compared to only
381 a few hundred in Nöthig et al. (2020), where the *in situ* sampling is mostly limited to one
382 campaign each spring-summer season. Further, our boxes span the whole Siberian seas, whereas
383 the *in situ* measurements are located mostly in the northern parts of the shelves. Climatological
384 maps of TChla are included as S2 in the supplements).

385   We assess Particulate Organic Carbon (POC) in regional boxplots similar to Nöthig et al.
386 (2020) in Figure 3B, where POC represents the sum of the particulate carbon pools in our model,
387 i.e., phytoplankton carbon, detrital carbon, and carbon contained in TEP. POC predictions for the
388 100 m depth integral range from 0.2 to18.6 g m^{-2} (1st – 3rd quartile), with highest values in the
389 Barents Sea between 6.0-15.1 g m^{-2} and in the eastern Fram Strait with 4.7-18.6 g m^{-2}. As for
390 TChla, intermediate values of POC (0.2-14.3 g m^{-2}) are predicted for the western Fram Strait and
391 on the Siberian shelves. In the central Arctic basins, the amount of POC is low with 0.3 to
392 2.7 g m^{-2}. This is in good agreement with the observations of Nöthig et al. (2020), who measured
393 the highest POC median of 13 g m^{-2} in the eastern Fram Strait, alongside 5-8 g m^{-2} in the western
394 Fram Strait and on the Siberian shelves. The higher simulated values on the shelves might be
395 caused by including also their southern parts, whereas the measurements do not cover these
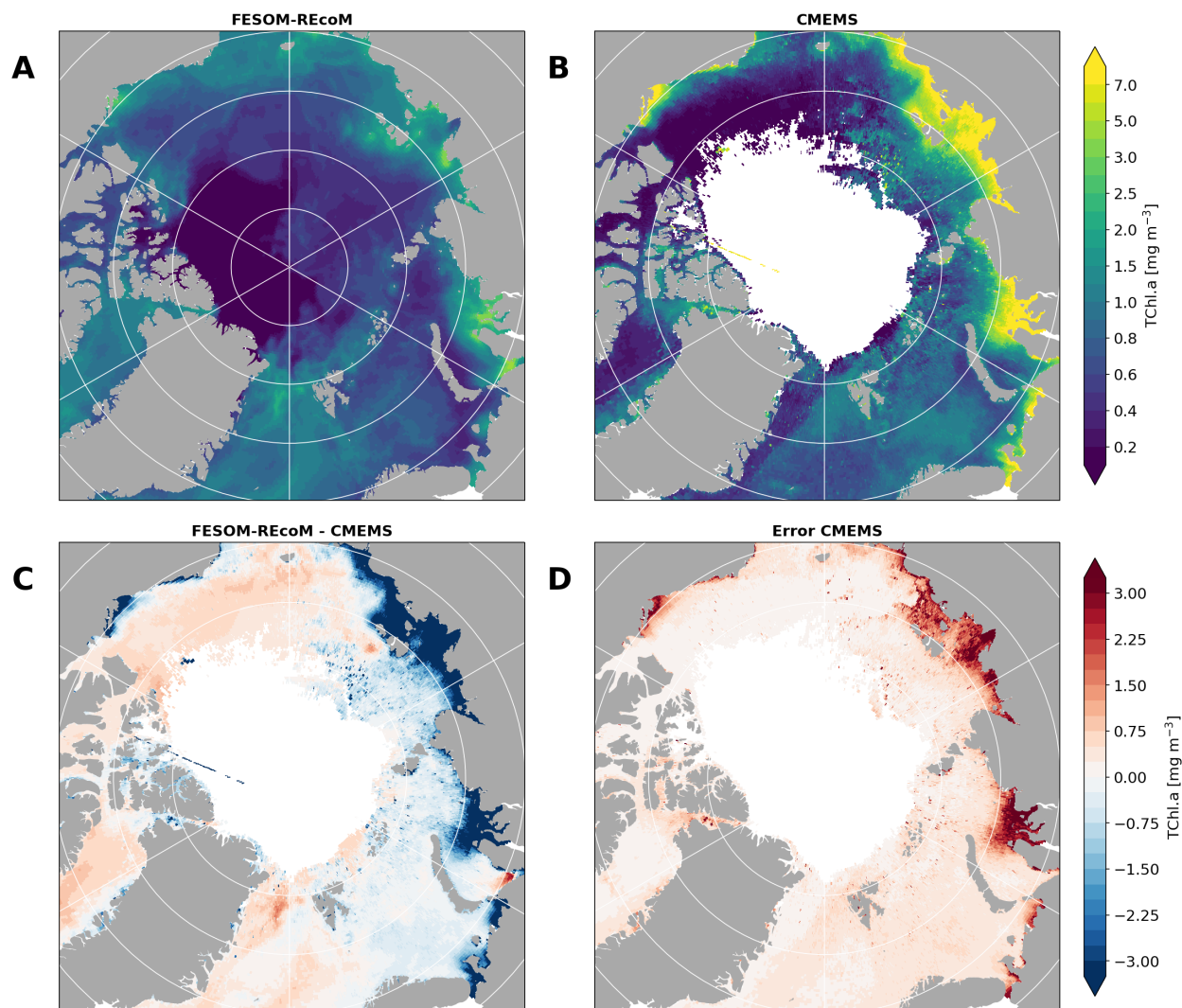396 areas.

397

398
399 **Figure 2**. Maps of surface Total Chlorophyll *a* (TChla) of FESOM-REcoM (A), of the CMEMS
400 Arctic re-analysis product (B), the difference of CMEMS to the model results (C), and the error
401 of CMEMS (D) as average of May to September over the years 2000-2019. CMEMS data does
402 not cover the central Arctic Ocean.
403

404
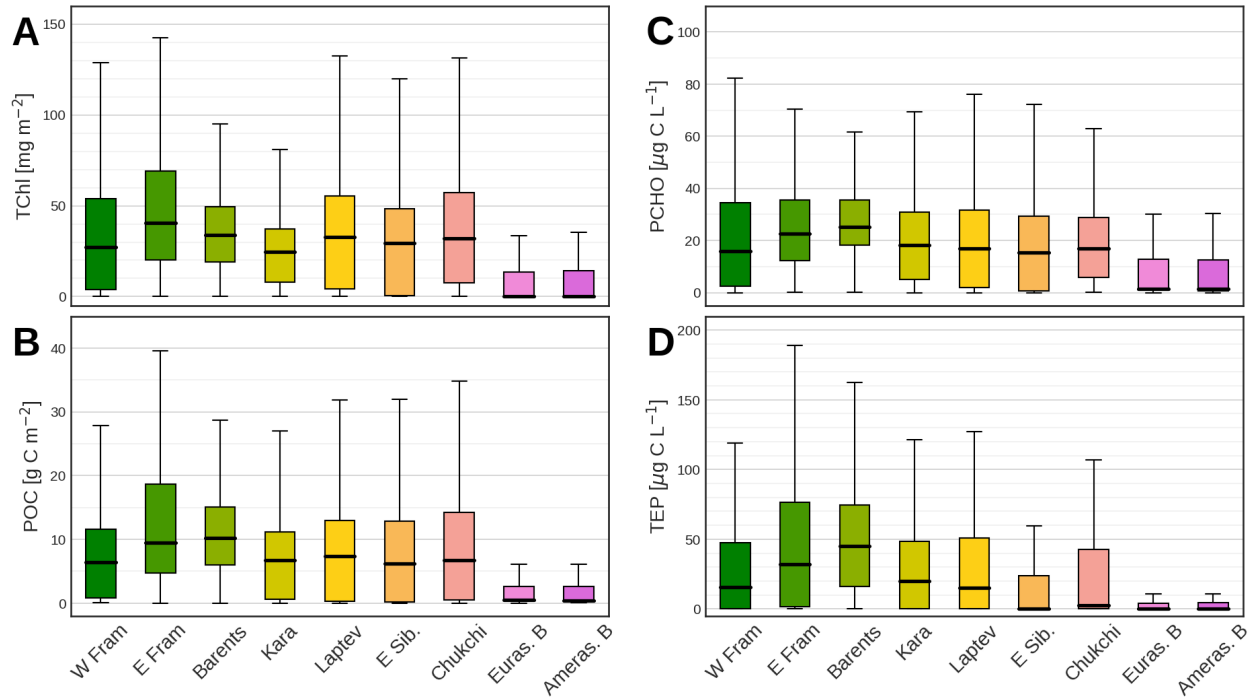405 **Figure 3**. Box plots comparing regional differences for Total Chlorophyll *a* (TChla, A),
406 Particulate Organic Carbon (POC, B), polysaccharides (PCHO, C), and of Transparent
407 Exopolymer Particles (TEP, D) following the region definitions mapped in Fig. 1 for western
408 Fram Strait (W Fram), eastern Fram Strait (E Fram), Barents Sea, Kara Sea, Laptev Sea, East
409 Siberian Shelves (E Sib), Chukchi Sea, Eurasian Basin (Euras. B), and Amerasian Basin
410 (Ameras. B.). Data is averaged over May to September of the 2000-2019 period, presented as
411 depth integrated (0-100 m) values for TChla and POC and volume-weighted mean (0-100 m) for
412 PCHO and TEP. The thick black line represents the median, the box represents the 1st and 3rd
413 quartile. The whiskers span over 1.5 times the inter-quartile range.

414   3.2 Arctic PCHO distribution and its link to a phytoplankton bloom in Fram Strait

415   We analyze in this section the relation of the phytoplankton bloom development with the
416 production of PCHO. Firstly, we analyze the long-term and spatially inclusive FESOM-REcoM
417 PCHO data which are presented as 0-100 m volume-weighted mean in Figure 3C, following the
418 presentation as done for TChla and POC. Our predictions are discussed alongside *in situ*
419 observations. Then we focus particularly on the Fram Strait to study the time evolution of
420 phytoplankton blooming in comparison to PCHO production in spatial context using our
421 FESOM-REcoM predictions. We conclude with a seasonal cycle of the phytoplankton phenology
422 to demonstrate the organic carbon flux from photosynthesis towards particle formation.

423   Regarding a regional overview, PCHO integrated over the upper 100 m is highest in the
424 Barents Sea with a median of 25.3 µg C L^{-1}, while in the Siberian seas, 15.5-18.2 µg C L^{-1} are
425 predicted. Eastern Fram Strait PCHO median concentration of 22.6 µg C L^{-1} is higher than
426 15.9 µg C L^{-1}in western Fram Strait (Figure 3C). For the Eurasian and Amerasian Basin, the
427 median ranges from 1.4-1.6 µg C L^{-1}. In eastern Fram Strait, von Jackowski et al. (2020) observe
428 DCCHO in concentrations of 55.8 µg C L^{-1} in July and 22.5 µgCL^{-1} in September (0-100 m),
429 which are slightly higher than FESOM-REcoM summer PCHO median (Fig. 3C). Piontek et al.

430 (2021) report decreasing concentration with depth for the Eurasian Basin, which we also observe
431 in our results, but to a much stronger extent. In the upper ocean, our model results fit to
432 observations by Piontek et al. (2021) in the Eurasian Basin, the northern Barents Sea, and
433 northern Laptev Sea, who measured 25.5-30.8 µg C L^{-1} DCCHO in the upper 40 m in August to
434 October 2012 (compared to 10-80 µg C L^{-1} of PCHO in this study, climatological maps for 0-
435 30 m volume-weighted mean are presented in Supplementary S3). Considering greater depths,
436 the volume-weighted median of 0-100 m depth of PCHO in FESOM-REcoM drops to 2 µg C L^{-1}
437 , while approx. 19-23 µg C L^{-1} DCCHO in the depth range 40-150 m are reported by Piontek et
438 al. (2021). The authors conducted their campaign in a year of extraordinary low sea-ice
439 concentration, which led to high TChla and a strong nutrient depletion. The high amounts of
440 DCCHO excreted by phytoplankton were not immediately turned over by bacterial activity and
441 could have accumulated in the water column as a result.

442 In order to analyze the link of phytoplankton bloom evolution and PCHO production, we
443 chose here the time period of May to July 2017 in analogy to the 2017 PASCAL campaign and
444 present predictions of sea-ice concentration, Dissolved Inorganic Nitrogen (DIN), TChla and
445 PCHO of the model's surface layer (0-5 m) in Figure 4. In the northern Atlantic and Arctic
446 Ocean phytoplankton growth predicted in our model is mostly limited by light. Early in the
447 season, sea-ice covers most parts of the Arctic Ocean and Fram Strait. In May of 2017, the
448 eastern Fram Strait is already ice-free (Fig. 4A). A phytoplankton bloom is formed in the
449 northern Atlantic and in the MIZ in the Fram Strait, most prominently along the ice edge (Fig.
450 4G – here defined as contour of 25% SIC). This bloom shifts further north into the whole eastern
451 Fram Strait in June, using up DIN. In the MIZ, high TChla of up to 6 mg m^{-3} is simulated. In
452 July, SIC decreases further and TChla is predicted in the whole Fram Strait, with a major
453 increase in the western part, and additionally in the northern Barents Sea (Fig 4C and I,
454 respectively).

455 Simulated PCHO follows elevated TChla first northward and then westward in the Fram
456 Strait area and reach surface concentration of up to 120 µg C L^{-1} (Fig. 4J, K, L), especially when
457 DIN is depleted (Fig. 4D, E, F). In May, PCHO concentrations are most elevated close to the ice
458 edge. In June, areas of elevated PCHO concentration are found towards the eastern Fram Strait
459 and Barents Sea. In July, PCHO concentrations peak in the MIZ of western Fram Strait and
460 northern Barents Sea alongside the phytoplankton blooms. Interestingly, there is a case where
461 high TChla does not result in high PCHO concentration: in June in the South-western Fram Strait
462 (Fig. 4K). DIN has not been used up completely in this area, hence, the phytoplankton is still not
463 suffering from nutrient depletion. The implemented limiter function for phytoplankton carbon
464 excretion (depending on the intracellular N:C ratio) is apparently still low, and as such, the
465 phytoplankton cells are not excreting excessive carbon to a large extent.

466 In the Fram Strait area, there is also a good agreement with PASCAL campaign data of
467 the same months of 2017, providing *in situ* measured concentrations of DCCHO in the open
468 ocean, marginal ice zone and ice-covered regions around Svalbard, despite the simulated PCHO
469 reflecting only a part of the DCCHO pool. Values were found to be lowest in the sea-ice leads
470 within ice-covered regions (11.3 ± 10.1 µg C L^{-1}). A similar concentration range can be observed
471 as well in the model results (Fig. 3). The PASCAL campaign data on DCCHO in the marginal
472 ice zone of 51.1± 37.0 µg C L^{-1} agree as well with the model results. In the ice-free ocean, mean
473 measured DCCHO concentration is 17.2 ± 5.2 µg C L^{-1}. In May and June of the modeled year
474 2017, high TChla concentrations are found in the ice-free ocean together with high DCCHO

475   concentration. In July, DCCHO concentration is still elevated even as TChla concentration has
476   declined. This might be caused by increased nutrient depletion of phytoplankton and therefore,
477   increase release of dissolved organic carbon following the carbon overconsumption hypothesis.

478   In order to assess the mean seasonal cycle over the years 2000-2019, phytoplankton
479   carbon, TChla, PCHO, and TEP (the later discussed in Section 3.3) concentrations are compiled
480   as a volume-weighted mean of the upper 30 m of the ocean for the eastern Fram Strait (Fig. 5).
481   The twenty year climatology shows that the seasonal dynamic of TChla and PCHO follows in
482   this region as is discussed explicitly in Figure 4 for 2017 for the surface waters. The
483   phytoplankton carbon concentration increases to a peak of approximately 160 µg C L^{-1} in July
484   likewise TChla, with highest concentrations of 1.5 mg L^{-1}. DIN concentration decreases from a
485   winter average of about 4 mmol m^{-3} with the start of the phytoplankton bloom in May to 1
486   mmol m^{-3} in August. Following the bloom closely in time, PCHO is released by phytoplankton
487   and its concentration rises to a maximum of approx. 25 µg C L^{-1} in July. In the following,
488   months, PCHO concentration declines, whereas TEP concentration rises quickly from May to
489   August to approx. 150 µg C L^{-1}, lagging approx. one month behind the phytoplankton bloom.

490   Overall, our PCHO prediction display that high PCHO are clearly linked to high TChla
491   concentrations coinciding with nutrient depletion in the open ocean and in the MIZ (e.g., July
492   2017 in West Fram Strait, Fig. 4). Furthermore, our model results show that PCHO is not
493   accumulated to a large extent in the upper ocean, but quickly aggregated to TEP.
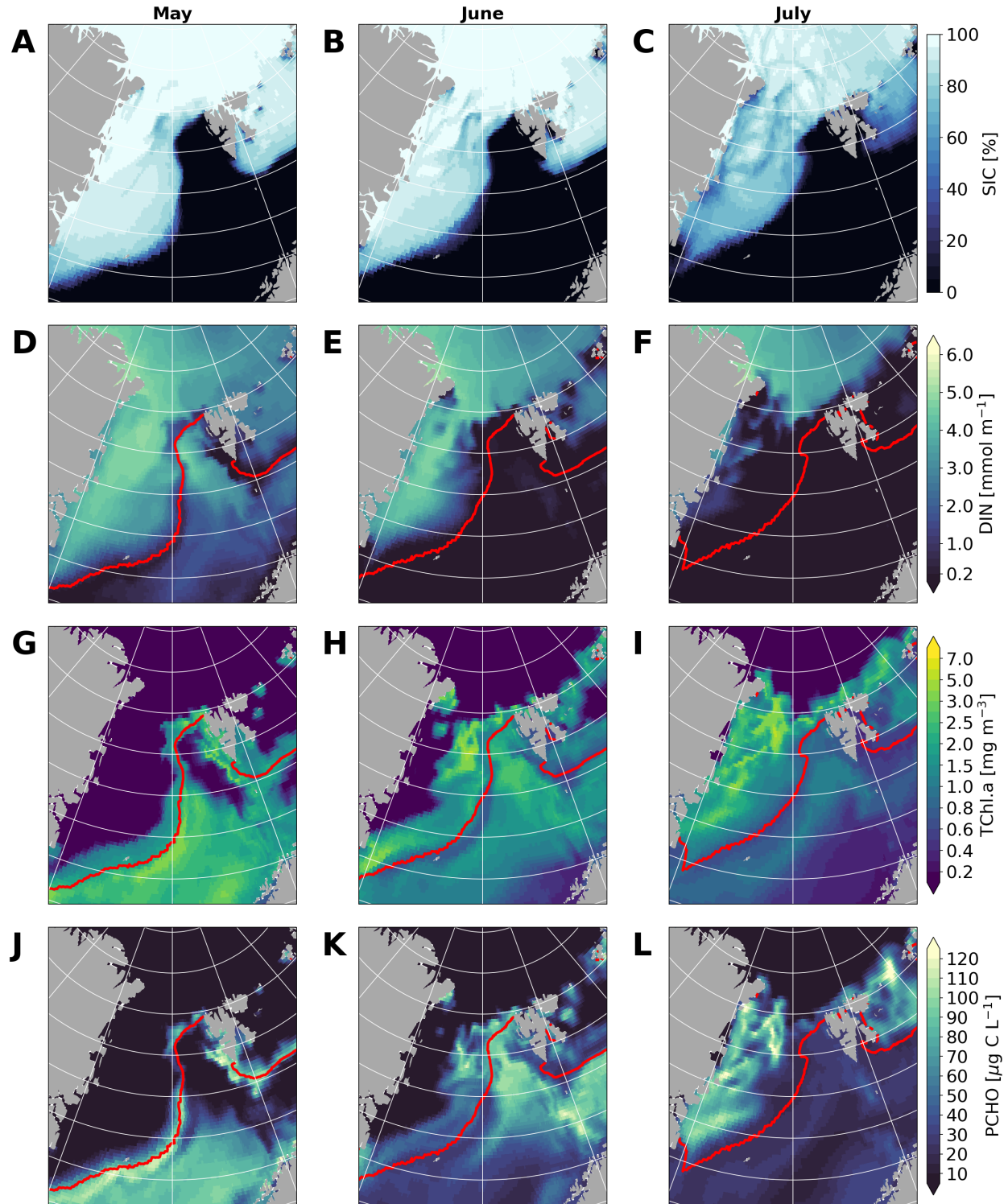
Figure 4. Maps of simulated sea-ice concentration (SIC, A-C), Dissolved Inorganic Nitrogen (DIN, D-F), Total Chlorophyll *a* (TChla, G-I) and polysaccharides (PCHO, J-L) as monthly mean of May, June, and July 2017 for the model's surface layer (0-5 m). The contour of the sea-ice edge (defined as 25% SIC) is depicted as red contour line.
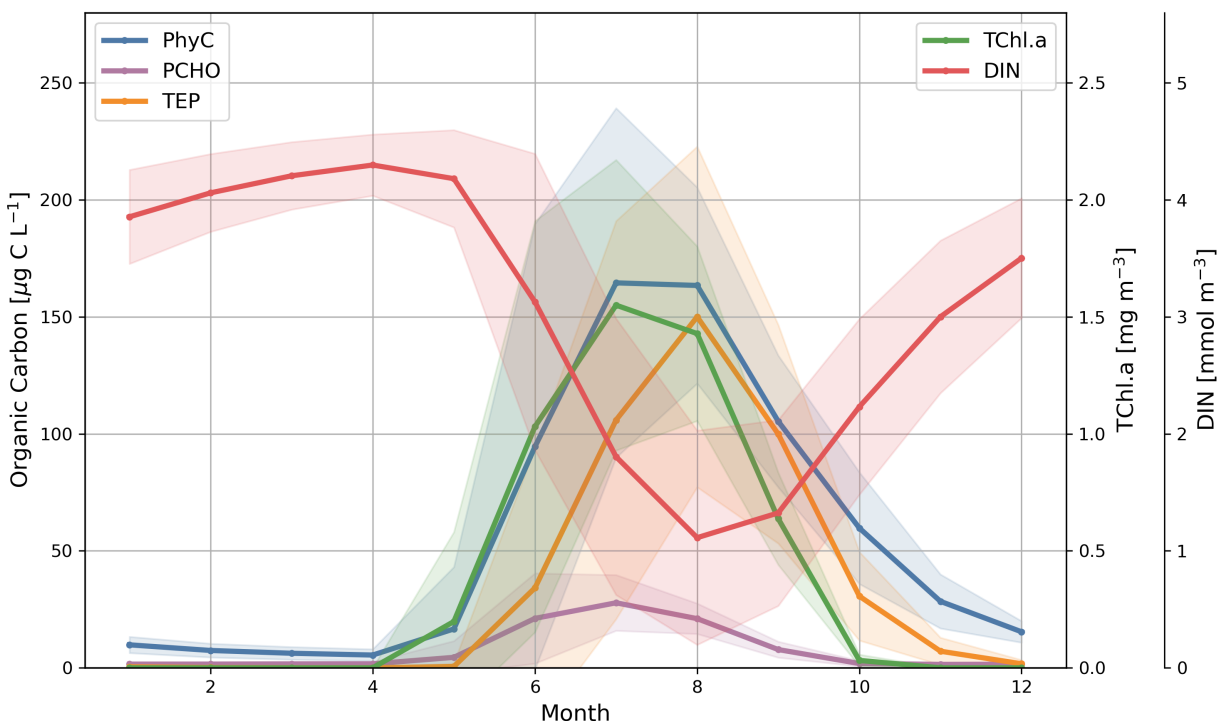
Figure 5. Seasonal cycle of simulated organic carbon of phytoplankton (blue), dissolved carboxylic acid containing polysaccharides (PCHO, purple), Transparent Exopolymer Particles (TEP, orange), on the left axis, and Total Chlorophyll *a* (TChla, green), and Dissolved Inorganic Nitrogen (DIN, red) on the right axis of the period 2000-2019 as volume-weighted mean of the upper 30 m ocean depth, averaged over the eastern Fram Strait (extent see Fig. 1). Standard deviation of the regional average is shown as shaded area in corresponding colors.

3.3 Occurrence of TEP in the Arctic

In this section we assess the prediction of TEP in the Arctic Ocean by describing its seasonal cycle in the Fram Strait, before broadening the perspective to an Arctic-wide climatology.

Following the other FESOM-REcoM variable presentations for the Fram Strait in Figure 5, also the TEP predictions exhibit a clear seasonal cycle in succession of the phytoplankton bloom (Fig. 5). In addition, Figure 5 shows that PCHO release and TEP production also depend on nutrient depletion during the bloom. This is in accordance with Engel et al. (2017) who found that TChla alone is not a good predictor for TEP in the Fram Strait. In the same region, Engel et al. (2017) also reported a strong link between TEP and phytoplankton occurrence patterns. Especially with respect to *Phaeocystis* spp., Zamanillo et al. (2019) found TEP concentration positively correlated to phytoplankton biomass along a wide transect in the Atlantic Ocean. Aggregation processes of PCHO lead to the formation of TEP, which itself further intensifies aggregation processes. According to the model formulation, the more TEP is present, the faster the aggregation process becomes.

Based on the Arctic-wide simulation, we produce monthly climatological maps of TEP for April to November and for a water depth of 0-30 m, roughly corresponding to the summer mixed layer depth in the Arctic Ocean (Peralta-Ferriz & Woodgate, 2015) (Fig. 6). In May, TEP

525 concentrations rise first in regions with phytoplankton blooms (c.f. monthly climatology of
526 TChla and PCHO in Supplementary Material S2, S3), i.e., in Fram Strait and on the shelves (50-
527 150 µg C L^{-1}). The climatology further shows that from June to August, TEP increases in the
528 Fram Strait, on the Siberian shelves, in the Chukchi and Beaufort Sea and reaches approx. 200-
529 400 µg C L^{-1}. TEP is also transported across the Arctic Ocean. As a result, the mean
530 concentration in the central Arctic Ocean reaches 10-50 µg C L^{-1} in the upper 30 m of the water
531 column. There is a gradient of TEP from the shelves towards the Arctic Ocean basins during
532 summer in our simulation. Yamada et al. (2015) highlight this gradient in their study on the
533 Chukchi shelf and Canadian basin (shelf 138.9±64.7 µg C L^{-1} to slope/basin: 79.3±15.5 µg C L^{-1},
534 0-50 m) and attribute it to TChla co-occurrence, transport from the shelf towards the basin, and
535 additional TEP production by prokaryotes. With the beginning of September, TEP declines in the
536 whole Arctic realm. Then, TEP is remineralized or descends to deeper ocean layers, and surface
537 concentrations decline. A rise in summer and quick decline in autumn is in accordance with TEP
538 observation data sets of von Jackowski et al., 2020 (21.4 ± 14.5 µg C L^{-1} in July, 7.1
539 ± 5.2 µg C L^{-1} in September, 0-100 m).

540 Table 2 compares our model TEP results for the Artic Ocean to observations averaged to
541 the same month and for the same depth range as provided by the *in situ* data: Considering the
542 comparison of point observations towards monthly integrated simulations for a small area,
543 overall, there is a good agreement, despite modeled TEP concentrations being often slightly
544 higher and differing particularly in the region of the Catlin Ice Base. Here, Wurl et al. (2011)
545 obtained their measurements from an under-ice phytoplankton bloom which resulted in very high
546 production of TEP. Such an event is not reproducible by FESOM-REcoM because ice-algae are
547 not explicitly modeled, and light-through-ice-transmission is not adequately represented.

548 For completeness to assess regional budgets, the TEP volume-weighted median
549 concentrations of 0-100 m are compiled as for PCHO in Figure 3D. The highest median of
550 44.9 µg C L^{-1} is reached in the Barents Sea. In the eastern Fram Strait, the median lies at
551 31.8 µg C L^{-1}, whereas in the western Fram Strait, Kara and Laptev Sea, median concentration of
552 15.3-19.8 µg C L^{-1} are predicted. In the East Siberian and Chukchi Sea, as well as in the Eurasian
553 and Amerasian Basin, median TEP concentration are below 3 µg C L^{-1}. Maxima of simulated
554 TEP values nearly reach 190 µg C L^{-1} in the western Fram Strait.

555 3.4 Decadal trends in summer TEP concentration

556 We estimated the linear trend of TEP concentrations for the months April to June and
557 July to September of the period 1990-2019 for the upper 30 m of the water column in the Arctic
558 regionally (Fig. 7). Interannual regional variations of TEP are high in our simulation but have
559 also been identified in observations. For example, in eastern Fram Strait, Engel et al. (2017)
560 found a spread of 3-310 µg C L^{-1} for 2009-2014. To our knowledge, other long-term trends of
561 TEP occurrence in the Arctic have not yet reported in observational studies. For early summer,
562 TEP trends are only significant for the regions Amerasian Basin (+9.8% yr^{-1}), Canadian
563 Archipelago (+7.4% yr^{-1}), Chukchi Sea (+3.3% yr^{-1}) as a whole (defined in Fig. 1, statistics in
564 Tab. S4 in the Supplementary) and other, smaller areas displayed in Figure 7, of which the most
565 prominent is a decrease located in the southern Barents Sea (-0.5-1.5 µg C L^{-1} yr^{-1}), as well as an
566 increase in the Barents Sea opening (0.5-1.0 µg C L^{-1} yr^{-1}) and in the Kara Sea close to the
567 Yenisey river mouth (0.5-3.0 µg C L^{-1} yr^{-1}). The area of significance of these trends is limited
568 (hatched in Fig. 7), but we note a slight positive trend across large parts of the Arctic Ocean

569   (< 0.5 µg C L^{-1} yr^{-1}). Interestingly, the wide-spread positive trend in early summer manifests
570   itself in the later summer months more prominently in the Kara Sea, the Canadian Archipelago,
571   the Amerasian Basin (significant trend across the whole three regions with +0.8% yr^{-1},
572   +1.2% yr^{-1}, +3.5% yr^{-1} correspondingly), and in a significant positive trend in parts of the East
573   Siberian, eastern Laptev, Chukchi, and Beaufort Seas (0.5-3 µg C L^{-1} yr^{-1}). Contrasting, a
574   significant negative trend develops in the eastern Fram Strait (-0.4% yr^{-1}) and in the Barents Sea
575   (-0.3% yr^{-1}), and in parts in the Eurasian Basin (< -0.75 µg C L^{-1} yr^{-1}). The simulated TEP trend
576   prediction splits into two major regions: one with Atlantic water influence (Fram Strait, Barents
577   Sea, parts of the Eurasian basin) with mainly a decrease of TEP, the other with Pacific water
578   influence (Beaufort Sea, Chukchi Sea, parts of the Amerasian basin) exhibiting a prominent
579   increase of TEP. Figure 5 illustrates that TEP occurrence follows phytoplankton blooms in the
580   eastern Fram Strait with a temporal lag of approx. one month, but also depends on the nutrient
581   limitation during blooming. In our simulation, Net Primary Production (NPP) generally increases
582   from 1990-2019 with exception of the Barents Sea and parts of the Eurasian Basin (Fig. 7C, D),
583   whereas nutrient availability decreases in the whole Arctic Ocean (data not shown), most
584   strongly in the Laptev, East Siberian and Beaufort Sea. Hence in the regions of Atlantic water
585   influence, the simulated significant decrease of NPP together with only a slight decrease of
586   nutrient availability might result in less carbon overflow from phytoplankton production and,
587   therefore, in the decrease of TEP concentration there. In contrast in the Laptev, East Siberian,
588   Chukchi and Beaufort Sea, the simulated NPP increases significantly, in hand with a significant
589   decrease of DIN, which results in the significant increase of simulated TEP concentration. NPP
590   has been shown to increase significantly in all regions of the Arctic Ocean and seas, most
591   strongly pronounced in the Kara, Laptev and Siberian Sea based on remote-sensing products
592   (Lewis et al., 2020). Lewis et al. (2020) argued that the increase of NPP results from enhanced
593   supply by nutrients. As a result of the diminishing sea-ice, light limitation is expected to decrease
594   further in the Central Arctic Ocean, shifting the phytoplankton more towards a nutrient-limited
595   regime (Oziel et al., 2022). Based on observations, Randelhoff et al. (2020) expect a wide-spread
596   nitrogen limitation across the Arctic except for the central basins. In contrast, Oziel et al. (2022)
597   predict from ocean biogeochemical modeling, that there is a nutrient limitation in the central
598   Arctic Ocean prevailing, as DIN supply through upwelling and lateral mesoscale eddy transport
599   does not suffice to replenish the reservoir.

600   Overall, we have shown that our model is capable to simulate well the TEP distributions
601   in the Arctic Ocean. As this is a first step to simulate TEP in the Arctic Ocean, the full
602   complexity of TEP cycling is not yet represented in the model: Other processes of the life cycle
603   of TEP such as ballasting of TEP and consecutive sinking in the water column, or
604   microbial/zooplankton grazing on the particles itself have not yet been implemented.
605   Additionally, Galgani et al., (2016) describe high numbers of TEP and its precursors in melt
606   ponds and open water of the central Arctic Ocean and argue, that TEP could also be released
607   from melting sea-ice. Still, the peak concentration values of TEP in FESOM-REcoM, especially
608   regarding the surface values, might be too high. A reason could be the missing transfer of
609   particles into the sea-surface microlayer (SML) in our simulation. The SML is the very thin
610   transition film at the ocean-atmosphere interface, which is not part of the model structure. TEP is
611   positively buoyant, thus, the particles would ascend through the water column and get enriched
612   in this layer (Azetsu-Scott & Passow, 2004; Wurl et al., 2011). In a methodological study,
613   Robinson et al. (2019) demonstrate the enrichment of TEP additionally via bubble scavenging, a
614   process when rising air bubbles transport organic matter. Observational studies report contrasting

615 results on SML enrichment. Galgani et al., (2016) report only minor enrichment in the surface
616 microlayer in the open water of the Central Arctic, whereas Wurl et al. (2011) calculated an
617 enrichment factor of 1.7±0.5 in the Canadian Arctic. One could use these enrichment factors for
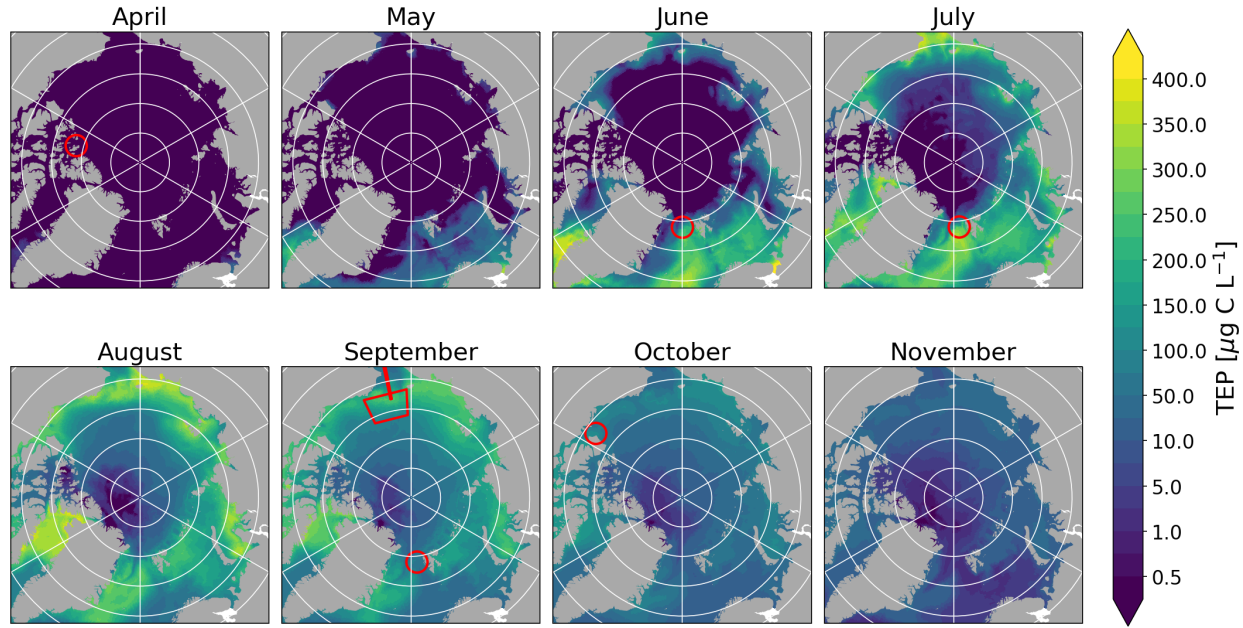618 our simulations to retrieve an estimate of TEP concentration in the SML.

619
620 **Figure 6**. Climatological maps of Transparent Exopolymer Particles (TEP) concentration as
621 volume-weighted mean of the upper 30 m of the simulated period 2000-2019. Overlayed are the
622 positions of the observation data points in red (c.f. Tab. 2).

623 **Table 2.** Comparison of carbon concentration of TEP (TEP-C) of observational campaigns and
624 simulation. Model results are volume-weighted and averaged corresponding to the depth range,
625 area, and month of observations. A variable number N of model grid cells was chosen to best fit
626 the area coverage of observations. Mean and standard deviation of the years 2000-2019 is stated
627 in brackets.

Period	Region	Depth [m]	Modeled TEP-C [µg C L^{-1}]	Observed TEP-C [µg C L^{-1}]	Number of Samples	Reference
Mar-Apr 2010	Catlin Ice Base	0-14	0±0 (0±0)	405.9±344.7	65	Wurl et al. (2011)
Jun 2015	Fram Strait	5-200	16.0±11.3 (20.9±16.6)	8.2±6.1	935	Engel et al. (2020)
Jul 2018	Fram Strait	0-100	102.9±23.5 (88.4±35.3)	21.4±14.5	1631	von Jackowski et al. (2020)
Sep-Oct 2018	Fram Strait	0-100	32.3±7.5 (27.7±11.6)	7.1±5.2	2440	von Jackowski et al. (2020)
Sep-Oct 2012	Chukchi Shelf	0-50	115.3±72.6 (77.5±46.9)	138.9±64.7	1106	Yamada et al. (2015)
Sep-Oct 2012	Canada Basin	0-200	29.2±6.9 (23.8±11.0)	70.4±15.5	14940	Yamada et al. (2015)

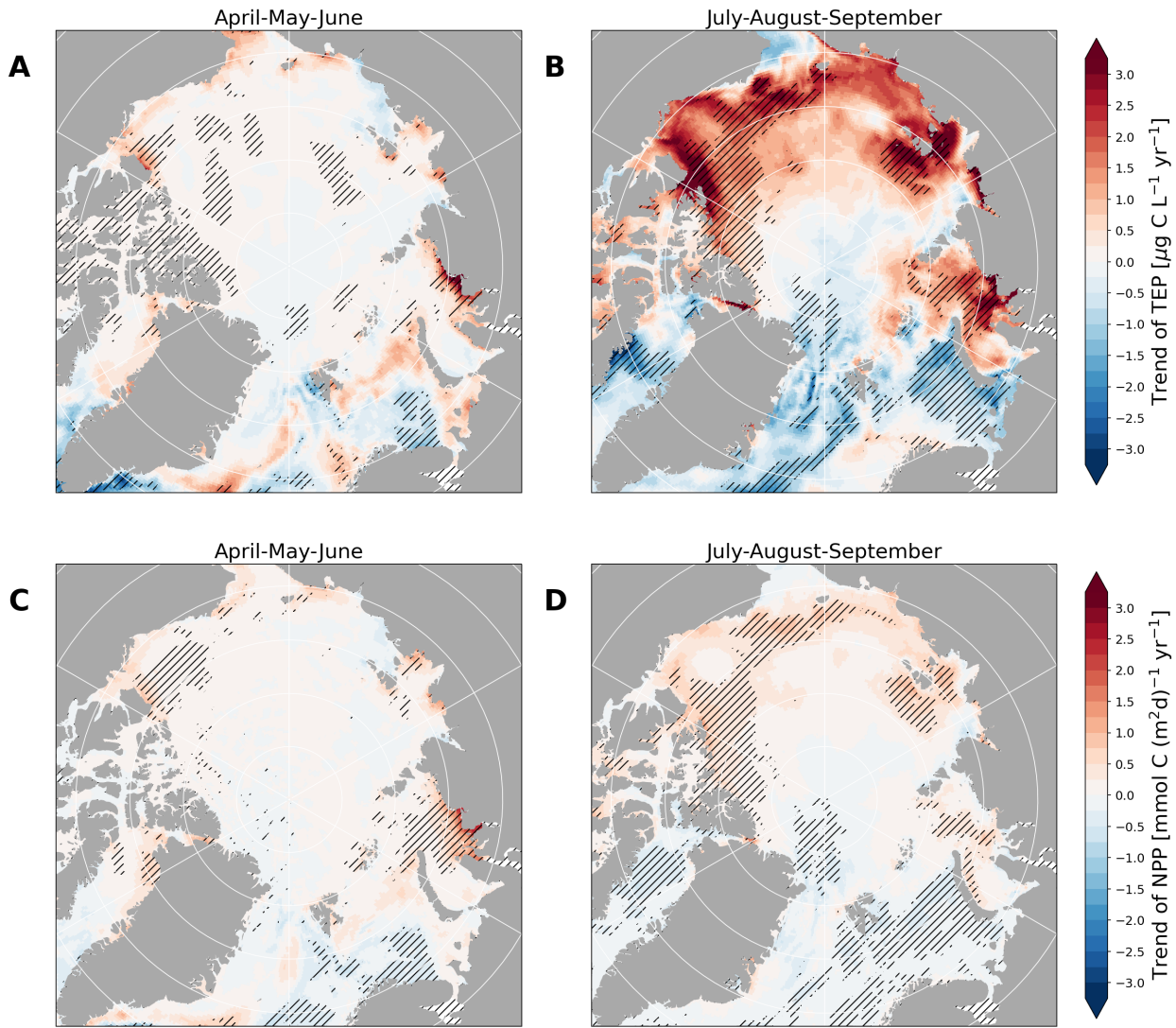| Oct 2009	Northwest Passage	0-29	137.0±12.1 (108.0±33.0)	126.1±69.7	174	Wurl et al. (2011)

628
629

Figure 7. Maps of the trend of the volume-weighted mean TEP concentration (0-30 m) of the months April-June (A) and July-September (B) and trend of Net Primary Production (NPP) for the same months (C, D) of the simulated period 1990-2019 as volume-weighted mean of the upper 30 m. Significant trends are displayed as hatched areas.

3.5 Global TEP patterns

As detailed in section 2.3, our new FESOM-REcoM setup was optimized in its parametrization and irregular grid to enable reliable Arctic sub-mesoscale predictions of PCHO and TEP. However, since FESOM-REcoM is a global model in principle, we additionally evaluate the TEP concentration in perspective to its global pattern. Because *in situ* observations are available mostly for surface waters (see review by Wurl & Cunliffe, 2017; updated by

642 Zamanillo et al.; 2019), we present here the model results as volume-weighted mean of the upper
643 30 m of the ocean averaged over 2000 – 2019. For completeness, global model results of TChla
644 and PCHO can be found as Supplementary Figures S5 and S6. Further, mean TEP concentrations
645 are also summarized by binning for each Longhurst Provinces (Longhurst, 2006), presented as
646 Table S7 in the Supplementary.

647   In large areas of the global ocean, simulated TEP concentration in FESOM-REcoM range
648 from 5-50 µg C L^{-1} (Fig. 8A). TEP concentrations are especially high in the Nordic Seas and the
649 Arctic Ocean with approx. 75-150 µg C L^{-1}. In the region of the Antarctic Polar Front and in the
650 Peruvian upwelling, TEP concentrations reach a minimum with values below 5 µg C L^{-1}. The
651 standard deviation of monthly, volume-weighted mean TEP concentration is highest in the Arctic
652 region with approx. 50-150 µg C L^{-1}, while between 30°S-30°N, standard deviation is lowest
653 with less than 5 µg C L^{-1} (Fig. 8B).

654   Engel et al. (2020) propose three different ocean regimes of TEP occurrence, to which we
655 compare our model results: an oligotrophic regime, a polar regime, and an eastern boundary
656 upwelling regime. The first, oligotrophic regime, is characterized by low phytoplankton
657 productivity, which also results in low TEP concentrations. In large parts of the Atlantic, Pacific,
658 and Indian Ocean, the modeled TEP concentration ranges between 5 and 25 µg C L^{-1} in the
659 annual average, without a notable seasonal cycle. This agrees to *in situ* data: Data reviewed in
660 Zamanillo et al., (2019) supports this pattern with a range of 5-36 µg C L^{-1}. Particularly, in the
661 tropical Atlantic, the TEP concentration is low at approx. 5-10 µg C L^{-1} (Engel et al., 2020; Wurl
662 & Cunliffe, 2017).

663   According to Engel et al. (2020), within the second regime represented by the polar
664 regions, TEP accumulates in the upper ocean layer. The authors contribute this mainly to the
665 occurrence of the phytoplankton *Phaeocystis* spp. and microbial degradation focusing primarily
666 on proteinaceous compounds rather than on TEP. For the Arctic Ocean, we discussed simulated
667 TEP above (Section 3.3). In the Southern Ocean during the blooming period between December
668 and March, modeled TEP concentrations increase to up to approx. 150 µg C L^{-1}, agreeing well to
669 observational studies reporting values of 0-39 µg C L^{-1}, with higher values of approximately
670 200 µg C L^{-1} in Bransfield Strait (Engel et al., 2020; Wurl & Cunliffe, 2017; Zamanillo et al.,
671 2019).

672   As a third regime, the eastern boundary upwelling systems are described as highly
673 productive regimes, which also results in high TEP production in hand with fast particle sinking
674 because of ballasting (Engel et al., 2020). Engel et al. (2020) report TEP values of up to
675 85 µg C L^{-1} in the Mauritanian and 9 µg C L^{-1} in the Peruvian upwelling system. Higher TEP
676 amounts of up to 1200 µg C L^{-1} are reported for the California Currents (Zamanillo et al., 2019).
677 Our setup of FESOM-REcoM does not simulate these regions properly in terms of primary
678 productivity, and as a consequence, lacks this TEP pattern of eastern upwelling regimes as well.
679 Overall, our simulated global TEP patterns are in good agreement with observational studies and
680 can serve as a first milestone of modeling TEP in a large-scale ocean biogeochemical model.
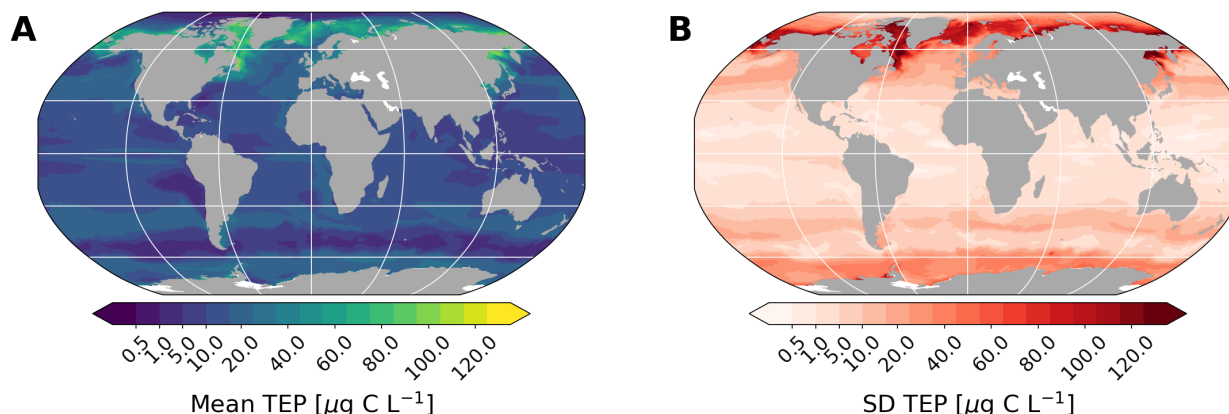
A

B

Mean TEP [μg C L^{-1}]

SD TEP [μg C L^{-1}]

Figure 8. Maps of global TEP concentration as volume-weighted mean of 0-30 m of the years 2000-2019 (A) and its standard deviation (SD) (B).

4 Conclusions

The formation of organic carbon by phytoplankton plays a key role in the dynamics of marine ecosystems. Within this work, we have introduced for the first time parametrizations into a coupled ocean biogeochemical model to enable realistic predictions of production of dissolved carboxylic acid containing polysaccharides (PCHO) and Transparent Exopolymer Particles (TEP). The new setup proved good agreement to field and remote sensing measurements of phytoplankton biomass in terms of TChla. Although our implementation of PCHO formation as fraction of excreted organic carbon, the consecutive aggregation to TEP, and its remineralization, are very simplified assumptions, we could show that the use of this parametrization resulted in realistic simulations of spatial and seasonal dynamics of TEP concentration for the Arctic compared to *in situ* observations.

We focused in this study on PCHO and TEP distribution in the upper 30 m of the ocean column, as we are interested mainly in providing an understanding of biogenic aerosol precursors in the Arctic. With mean concentrations of 100-400 µg C L^{-1} in the upper 30 m of the ocean, TEP is available as a large pool of biogenic aerosol precursors. The particle itself can either be directly transported into the atmosphere or serve as a tracer in our simulation for the presence of other biogenic compounds which were not directly simulated in our model. Our results can also serve as a first baseline for a global assessment of biogenic aerosol precursors, as TEP concentration within FESOM-REcoM is in reasonable agreement with observations. Still, our setup is tuned for the Arctic realm specifically and another setup as e.g., Gürses et al. (2023) might be more adapted when broadening the research question to a global level.

Furthermore, with our over 30 years TEP simulations, diverging trends become visible. In the Fram Strait, Barents Sea and in the Eurasian Basin, TEP concentrations mostly decline over time, whereas there is an increase in the other parts of the Arctic Ocean, which is strongest in the Kara, Laptev and Beaufort Sea. We linked this change in the first case to a decrease in NPP, whereas in the second case, NPP increases with coinciding decrease of available nitrate concentration in the upper 30 m of the water column. This leads to stronger nutrient limitation of phytoplankton growth and results in the excretion of organic carbon according to the carbon overflow hypothesis (Engel et al. 2020). Even more in a warming ocean, the excretion of

714 polysaccharides has been suggested to increase (Engel et al., 2011), which could enhance the
715 production of TEP as well.

716   Finally, this simulation can serve as an ocean component in Earth System Models to
717 estimate the fluxes of biogenic aerosol precursors from the upper ocean into the atmosphere.
718 TEP itself, but also other biogenic particles derived from the model output, can serve to better
719 describe cloud formation and its microphysical properties in an atmospheric model. In this way,
720 this study contributes to a better understanding of aerosol feedbacks in the Arctic realm.

740

Data availability

741

FESOM2.1-REcoM3 model source code is accessible at https://github.com/FESOM/fesom2. The

743 curated simulation results are available at https://doi.org/10.5281/zenodo.7886868 (Zeising et al.,

744 2023). The evaluation of model output was done using python3 (Python Software Foundation) and

745 the modules pyfesom2 (https://github.com/FESOM/pyfesom2) and py_f2recom (not published,

746 Maresys group, AWI), which are based on xarray, scipy, cartopy, and matplotlib, among others.

747 Observation data sets for model evaluation were obtained directly from the cited literature. The

748 Copernicus Marine Environment Monitoring Service level 4 monthly reprocessed Ocean Color

749 product (Product ID: OCEANCOLOUR_ARC_BGC_L4_MY_009_124) was obtained from

750 Copernicus Marine Data Store at

751 https://data.marine.copernicus.eu/product/OCEANCOLOUR_ARC_BGC_L4_MY_009_124/. The

752 Arctic Ocean TChla product presented in Lewis et al. (2020) was downloaded from Stanford Digital

753 Repository at https://doi.org/10.25740/kc822vj3040. The data set on DCCHO used in Jackowski et

754 al. (2020) is as well published at https://doi.pangaea.de/10.1594/PANGAEA.915751. The DCCHO

755 data set of the PASCAL campaign on RV Polarstern is available at PANGAEA (Zeppenfeld et al.,

756 2023). The Longhurst provinces were provided as shapefile by marineregions.org (Flanders Marine

757 Institute, 2009).

758

References

760 Alldredge, A. L., & Crocker, K. M. (1995). Why do sinking mucilage aggregates accumulate in

761 the water column? *Science of The Total Environment*, *165*(1), 15–22. doi:10.1016/0048-

762 9697(95)04539-D

763   Alldredge, A. L., Passow, U., & Logan, B. E. (1993). The abundance and significance of a class

764   of large, transparent organic particles in the ocean. *Deep Sea Research Part I: Oceanographic*

765   *Research Papers*, *40*(6), 1131–1140. doi:10.1016/0967-0637(93)90129-Q

766   Aller, J. Y., Radway, J. C., Kilthau, W. P., Bothe, D. W., Wilson, T. W., Vaillancourt, R. D., et

767   al. (2017). Size-resolved characterization of the polysaccharidic and proteinaceous components

768   of sea spray aerosol. *Atmospheric Environment*, *154*, 331–347.

769   doi:10.1016/j.atmosenv.2017.01.053

770   Álvarez, E., Thoms, S., Bracher, A., Liu, Y., & Völker, C. (2019). Modeling Photoprotection at

771   Global Scale: The Relative Role of Nonphotosynthetic Pigments, Physiological State, and

772   Species Composition. *Global Biogeochemical Cycles*, *33*. doi:10.1029/2018GB006101

773   von Appen, W.-J., Waite, A. M., Bergmann, M., Bienhold, C., Boebel, O., Bracher, A., et al.

774   (2021). Sea-ice derived meltwater stratification slows the biological carbon pump: results from

775   continuous observations. *Nature Communications*, *12*(1), 7309. doi:10.1038/s41467-021-26943-

776   z

777   Ardyna, M., & Arrigo, K. R. (2020). Phytoplankton dynamics in a changing Arctic Ocean.

778   *Nature Climate Change*, *10*(10), 892–903. doi:10.1038/s41558-020-0905-y

779   Arrigo, K. R., Perovich, D. K., Pickart, R. S., Brown, Z. W., van Dijken, G. L., Lowry, K. E., et

780   al. (2014). Phytoplankton blooms beneath the sea ice in the Chukchi Sea. *Deep Sea Research*

781   *Part II: Topical Studies in Oceanography*, *105*, 1–16.

782   Assmy, P., Fernández-Méndez, M., Duarte, P., Meyer, A., Randelhoff, A., Mundy, C. J., et al.

783   (2017). Leads in Arctic pack ice enable early phytoplankton blooms below snow-covered sea ice.

784   *Scientific Reports*, *7*, 40850.

785   Ayers, G. P., & Cainey, J. M. (2008). The CLAW hypothesis: a review of the major

786   developments. *Environmental Chemistry*, *4*(6), 366–374. doi:10.1071/EN07080

787   Azetsu-Scott, K., & Passow, U. (2004). Ascending marine particles: Significance of transparent

788   exopolymer particles (TEP) in the upper ocean. *Limnology and Oceanography*, *49*(3), 741–748.

789   doi:10.4319/lo.2004.49.3.0741

790   Bélanger, S., Babin, M., & Tremblay, J.-E. (2013). Increasing cloudiness in Arctic damps the

791   increase in phytoplankton primary production due to sea ice receding. *Biogeosciences*, *10*, 4087–

792   4101.

793   Block, K., Schneider, F. A., Mülmenstädt, J., Salzmann, M., & Quaas, J. (2020). Climate models

794   disagree on the sign of total radiative feedback in the Arctic. *Tellus A: Dynamic Meteorology*

795   *and Oceanography*, *72*(1), 1–14. doi:10.1080/16000870.2019.1696139

796   Charlson, R. J., Lovelock, J. E., Andreae, M. O., & Warren, S. G. (1987). Oceanic

797   phytoplankton, atmospheric sulphur, cloud albedo and climate. *Nature*, *326*(6114), 655–661.

798   doi:10.1038/326655a0

799   Cherkasheva, A., Bracher, A., Melsheimer, C., Köberle, C., Gerdes, R., Nöthig, E.-M., et al.

800   (2014). Influence of the physical environment on polar phytoplankton blooms: A case study in

801   the Fram Strait. *Journal of Marine Systems*, *132*, 196–207. doi:10.1016/j.jmarsys.2013.11.008

802   Copernicus Marine Service, & PML. (2022). Arctic Ocean Colour Plankton Multi-Year L4 daily

803   climatology and monthly observations [Data set]. Mercator Ocean International.

804   doi:10.48670/MOI-00293

805   Danilov, S., Sidorenko, D., Wang, Q., & Jung, T. (2017). The Finite-volumE Sea ice–Ocean

806   Model (FESOM2). *Geosci. Model Dev.*, *10*, 765–789. doi:10.5194/gmd-10-765-2017

807   Ebell, K., Nomokonova, T., Maturilli, M., & Ritter, C. (2020). Radiative Effect of Clouds at Ny-

808   Ålesund, Svalbard, as Inferred from Ground-Based Remote Sensing Observations. *Journal of*

809   *Applied Meteorology and Climatology*, *59*(1), 3–22. doi:10.1175/JAMC-D-19-0080.1

810   Engel, A. (2009). Determination of Marine Gel Particles. In *Practical Guidelines for the*

811   *Analysis of Seawater* (pp. 125–142). Boca Raton, USA: CRC-Press. Retrieved from

812   http://dx.doi.org/10.1201/9781420073072.ch7

813   Engel, A., Thoms, S., Riebesell, U., Rochelle-Newall, E., & Zondervan, I. (2004).

814   Polysaccharide aggregation as a potential sink of marine dissolved organic carbon. *Nature*,

815   *428*(6986), 929–932. doi:10.1038/nature02453

816   Engel, A., Händel, N., Wohlers, J., Lunau, M., Grossart, H.-P., Sommer, U., & Riebesell, U.

817   (2011). Effects of sea surface warming on the production and composition of dissolved organic

818   matter during phytoplankton blooms: results from a mesocosm study. *Journal of Plankton*

819   *Research*, *33*(3), 357–372. doi:10.1093/plankt/fbq122

820   Engel, A., Piontek, J., Metfies, K., Endres, S., Sprong, P., Peeken, I., et al. (2017). Inter-annual

821   variability of transparent exopolymer particles in the Arctic Ocean reveals high sensitivity to

822   ecosystem changes. *Scientific Reports*, *7*(1), 1–9.

823   Engel, A., Endres, S., Galgani, L., & Schartau, M. (2020). Marvelous Marine Microgels: On the

824   Distribution and Impact of Gel-Like Particles in the Oceanic Water-Column. *Frontiers in Marine*

825   *Science*, *7*, 405. doi:10.3389/fmars.2020.00405

826   Flanders Marine Institute. (2009). Longhurst Provinces. Retrieved from

827   https://www.marineregions.org/

828   Galgani, L., Piontek, J., & Engel, A. (2016). Biopolymers form a gelatinous microlayer at the

829   air-sea interface when Arctic sea ice melts. *Scientific Reports*, *6*, 29465. doi:10.1038/srep29465

830   Garcia, H., Weathers, K., Paver, C., Smolyar, I., Boyer, T., Locarnini, M., et al. (2019a). World

831   ocean atlas 2018. Vol. 4: Dissolved inorganic nutrients (phosphate, nitrate and nitrate+ nitrite,

832   silicate). *A. Mishonov Technical Editor, Tech. Rep.*, *NOAA Atlas NESDIS*(84).

833   Garcia, H., Weathers, K., Paver, C., Smolyar, I., Boyer, T., Locarnini, M., et al. (2019b). World

834   Ocean Atlas 2018, Volume 3: Dissolved Oxygen, Apparent Oxygen Utilization, and Dissolved

835   Oxygen Saturation. *A. Mishonov Technical Editor, Tech. Rep.*, *NOAA Atlas NESDIS*(83).

836   Goosse, H., Kay, J. E., Armour, K. C., Bodas-Salcedo, A., Chepfer, H., Docquier, D., et al.

837   (2018). Quantifying climate feedbacks in polar regions. *Nature Communications*, *9*(1), 1919.

838   doi:10.1038/s41467-018-04173-0

839   Gürses, Ö., Oziel, L., Karakus, O., Sidorenko, D., Völker, C., Ye, Y., et al. (2023). Ocean

840   biogeochemistry in the coupled ocean-sea ice-biogeochemistry model FESOM2.1-REcoM3.

841   *Geosci. Model Dev. Discuss.*, *2023*, 1–73. doi:10.5194/gmd-2023-2

842   Gürses, Özgür. (2021). FESOM2.1-REcoM2.1. *Geoscientific Model Development*.

843   Hartmann, M., Adachi, K., Eppers, O., Haas, C., Herber, A., Holzinger, R., et al. (2020).

844   Wintertime Airborne Measurements of Ice Nucleating Particles in the High Arctic: A Hint to a

845   Marine, Biogenic Source for Ice Nucleating Particles. *Geophysical Research Letters*, *47*(13),

846   e2020GL087770. doi:10.1029/2020GL087770

847   Hauck, J., Völker, C., Wang, T., Hoppema, M., Losch, M., & Wolf-Gladrow, D. A. (2013).

848   Seasonally different carbon flux changes in the Southern Ocean in response to the southern

849   annular mode. *Global Biogeochemical Cycles*, *27*(4), 1236–1245. doi:10.1002/2013GB004600

850   Hauck, J., Zeising, M., Le Quéré, C., Gruber, N., Bakker, D. C. E., Bopp, L., et al. (2020).

851   Consistency and Challenges in the Ocean Carbon Sink Estimate for the Global Carbon Budget.

852   *Frontiers in Marine Science*, *7*, 571720. doi:10.3389/fmars.2020.571720

853   Hawkins, L. N., & Russell, L. M. (2010). Polysaccharides, Proteins, and Phytoplankton

854   Fragments: Four Chemically Distinct Types of Marine Primary Organic Aerosol Classified by

855   Single Particle Spectromicroscopy. *Advances in Meteorology*, *2010*, 612132-.

856   doi:10.1155/2010/612132

857   Heim, B., Abramova, E., Doerffer, R., Günther, F., Hölemann, J., Kraberg, A., et al. (2014).

858   Ocean colour remote sensing in the southern Laptev Sea: evaluation and applications.

859   *Biogeosciences*, *11*(15), 4191–4210. doi:10.5194/bg-11-4191-2014

860   Hunke, E., Allard, R., Bailey, D. A., Blain, P., Craig, A., Dupont, F., et al. (2020, March). CICE-

861   Consortium/Icepack: Icepack 1.2.1 (Version 1.2.1). Zenodo. doi:10.5281/zenodo.3712299

862   Ingvaldsen, R. B., Assmann, K. M., Primicerio, R., Fossheim, M., Polyakov, I. V., & Dolgov, A.

863   V. (2021). Physical manifestations and ecological implications of Arctic Atlantification. *Nature*

864   *Reviews Earth & Environment*, *2*(12), 874–889. doi:10.1038/s43017-021-00228-x

865   Intrieri, J. M. (2002). An annual cycle of Arctic surface cloud forcing at SHEBA. *Journal of*

866   *Geophysical Research*, *107*(C10), 8039. doi:10.1029/2000JC000439

867   Irish, V. E., Elizondo, P., Chen, J., Chou, C., Charette, J., Lizotte, M., et al. (2017). Ice-

868   nucleating particles in Canadian Arctic sea-surface microlayer and bulk seawater. *Atmospheric*

869   *Chemistry and Physics*, *17*(17), 10583–10595. doi:10.5194/acp-17-10583-2017

870   von Jackowski, A., Grosse, J., Nöthig, E.-M., & Engel, A. (2020). Dynamics of organic matter

871   and bacterial activity in the Fram Strait during summer and autumn. *Philosophical Transactions*

872   *of the Royal Society A: Mathematical, Physical and Engineering Sciences*, *378*(2181), 20190366.

873   doi:10.1098/rsta.2019.0366

874   Janout, M. A., Hölemann, J., Waite, A. M., Krumpen, T., von Appen, W.-J., & Martynov, F.

875   (2016). Sea-ice retreat controls timing of summer plankton blooms in the Eastern Arctic Ocean.

876   *Geophysical Research Letters*, *43*(24), 12,493-12,501. doi:10.1002/2016GL071232

877   Jung, J., Lee, Y., Cho, K.-H., Yang, E. J., & Kang, S.-H. (2022). Spatial Distributions of

878   Riverine and Marine Dissolved Organic Carbon in the Western Arctic Ocean: Results From the

879   2018 Korean Expedition. *Journal of Geophysical Research: Oceans*, *127*(7), e2021JC017718.

880   doi:10.1029/2021JC017718

881   Karakuş, O., Völker, C., Iversen, M., Hagen, W., Gladrow, D. W., Fach, B., & Hauck, J. (2021).

882   Modeling the Impact of Macrozooplankton on Carbon Export Production in the Southern Ocean.

883   *Journal of Geophysical Research: Oceans*, *n/a*(n/a), e2021JC017315.

884   doi:10.1029/2021JC017315

885   Koldunov, N. V., Aizinger, V., Rakowsky, N., Scholz, P., Sidorenko, D., Danilov, S., & Jung, T.

886   (2019). Scalability and some optimization of the Finite-volumE Sea ice–Ocean Model, Version

887   2.0 (FESOM2). *Geoscientific Model Development*, *12*(9), 3991–4012. doi:10.5194/gmd-12-

888   3991-2019

889   Krembs, C., & Deming, J. W. (2008). The role of exopolymers in microbial adaptation to sea ice.

890   In *Psychrophiles: from biodiversity to biotechnology* (pp. 247–264). Springer.

891   Kwok, R. (2018). Arctic sea ice thickness, volume, and multiyear ice coverage: losses and

892   coupled variability (1958–2018). *Environmental Research Letters*, *13*(10), 105005.

893   doi:10.1088/1748-9326/aae3ec

894   Lauvset, S. K., Key, R. M., Olsen, A., van Heuven, S., Velo, A., Lin, X., et al. (2016). A new

895   global interior ocean mapped climatology: the 1° × 1° GLODAP version 2. *Earth Syst. Sci.*

896   *Data*, *8*(2), 325–340. doi:10.5194/essd-8-325-2016

897   Leck, C., & Bigg, E. K. (2007). A modified aerosol - cloud - climate feedback hypothesis.

898   *Environmental Chemistry*, *4*(6), 400.

899   Lewis, K. M., & Arrigo, K. R. (2020). Ocean Color Algorithms for Estimating Chlorophyll a,

900   CDOM Absorption, and Particle Backscattering in the Arctic Ocean. *Journal of Geophysical*

901   *Research: Oceans*, *125*(6), e2019JC015706. doi:10.1029/2019JC015706

902   Lewis, K. M., van Dijken, G. L., & Arrigo, K. R. (2020). Changes in phytoplankton

903   concentration now drive increased Arctic Ocean primary production. *Science*, *369*(6500), 198–

904   202. doi:10.1126/science.aay8380

905   Longhurst, A. R. (2006). *Ecological geography of the sea* (2nd Edition). San Diego: Academic

906   Press.

907   Macke, A., & Flores, H. (2018, June). The expeditions PS106/1 and 2 of the research vessel

908   POLARSTERN to the arctic ocean in 2017. Bremerhaven: Alfred Wegener Institute for Polar

909   and Marine Research. doi:10.2312/BzPM_0719_2018

910   Nöthig, E.-M., Bracher, A., Engel, A., Metfies, K., Niehoff, B., Peeken, I., et al. (2015).

911   Summertime plankton ecology in Fram Strait—a compilation of long- and short-term

912   observations. *Polar Research*, *34*(1), 23349. doi:10.3402/polar.v34.23349

913   Nöthig, E.-M., Ramondenc, S., Haas, A., Hehemann, L., Walter, A., Bracher, A., et al. (2020).

914   Summertime Chlorophyll a and Particulate Organic Carbon Standing Stocks in Surface Waters

915   of the Fram Strait and the Arctic Ocean (1991–2015). *Frontiers in Marine Science*, *7*, 350.

916   doi:10.3389/fmars.2020.00350

917   Ogawa, H., & Tanoue, E. (2003). Dissolved Organic Matter in Oceanic Waters. *Journal of*

918   *Oceanography*, *59*(2), 129–147. doi:10.1023/A:1025528919771

919   Orellana, M. V., Matrai, P. A., Leck, C., Rauschenberg, C. D., Lee, A. M., & Coz, E. (2011).

920   Marine microgels as a source of cloud condensation nuclei in the high Arctic. *Proc. Natl. Acad.*

921   *Sci.*, *108*(33), 13612–13617. doi:10.1073/pnas.1102457108

922   Oziel, L., Schourup-Kristensen, V., Wekerle, C., & Hauck, J. (2022). The Pan-Arctic Continental

923   Slope as an Intensifying Conveyer Belt for Nutrients in the Central Arctic Ocean (1985–2015).

924   *Global Biogeochemical Cycles*, *36*(6), e2021GB007268. doi:10.1029/2021GB007268

925   Pakulski, J. D., & Benner, R. (1994). Abundance and distribution of carbohydrates in the ocean.

926   *Limnology and Oceanography*, *39*(4), 930–940.

927   Park, J., Dall'Osto, M., Park, K., Kim, J.-H., Park, J., Park, K.-T., et al. (2019). Arctic Primary

928   Aerosol Production Strongly Influenced by Riverine Organic Matter. *Environmental Science &*

929   *Technology*, *53*(15), 8621–8630. doi:10.1021/acs.est.9b03399

930   Passow, U. (2002). Production of transparent exopolymer particles (TEP) by phyto- and

931   bacterioplankton. *Mar Ecol Prog Ser*, *236*, 1–12.

932   Peralta-Ferriz, C., & Woodgate, R. A. (2015). Seasonal and interannual variability of pan-Arctic

933   surface mixed layer properties from 1979 to 2012 from hydrographic data, and the dominance of

934   stratification for multiyear mixed layer depth shoaling. *Progress in Oceanography*, *134*, 19–53.

935   doi:10.1016/j.pocean.2014.12.005

936   van Pinxteren, M., Robinson, T.-B., Zeppenfeld, S., Gong, X., Bahlmann, E., Fomba, K. W., et

937   al. (2022). High number concentrations of transparent exopolymer particles in ambient aerosol

938   particles and cloud water – a case study at the tropical Atlantic Ocean. *Atmos. Chem. Phys.*,

939   *22*(8), 5725–5742. doi:10.5194/acp-22-5725-2022

940   Piontek, J., Galgani, L., Nöthig, E.-M., Peeken, I., & Engel, A. (2021). Organic matter

941   composition and heterotrophic bacterial activity at declining summer sea ice in the central Arctic

942   Ocean. *Limnology and Oceanography*, *66*(S1), S343–S362. doi:10.1002/lno.11639

943   Pithan, F., & Mauritsen, T. (2014). Arctic amplification dominated by temperature feedbacks in

944   contemporary climate models. *Nature Geoscience*, *7*(3), 181–184. doi:10.1038/ngeo2071

945   Pörtner, H.-O., Roberts, D., Masson-Delmotte, V., Zhai, P., Tignor, M., Poloczanska, E., et al.

946   (2019). The ocean and cryosphere in a changing climate. A special report of the

947   intergovernmental panel on climate change. *Intergovernmental Panel on Climate Change*, 1–

948   765.

949   Randelhoff, A., Holding, J., Janout, M., Sejr, M. K., Babin, M., Tremblay, J.-É., & Alkire, M. B.

950   (2020). Pan-Arctic Ocean Primary Production Constrained by Turbulent Nitrate Fluxes.

951   *Frontiers in Marine Science*, *7*, 150. doi:10.3389/fmars.2020.00150

952   Rantanen, M., Karpechko, A. Yu., Lipponen, A., Nordling, K., Hyvärinen, O., Ruosteenoja, K.,

953   et al. (2022). The Arctic has warmed nearly four times faster than the globe since 1979.

954   *Communications Earth & Environment*, *3*(1), 168. doi:10.1038/s43247-022-00498-3

955   Robinson, T.-B., Stolle, C., & Wurl, O. (2019). Depth is relative: the importance of depth for

956   transparent exopolymer particles in the near-surface environment. *Ocean Science*, *15*(6), 1653–

957   1666.

958   Robinson, T.-B., Giebel, H.-A., & Wurl, O. (2019). Riding the Plumes: Characterizing Bubble

959   Scavenging Conditions for the Enrichment of the Sea-Surface Microlayer by Transparent

960   Exopolymer Particles. *Atmosphere*, *10*(8), 454. doi:10.3390/atmos10080454

961   Schartau, M., Engel, A., Schröter, J., Thoms, S., Völker, C., & Wolf-Gladrow, D. (2007).

962   Modelling carbon overconsumption and the formation of extracellular particulate organic carbon.

963   *Biogeosciences Discussions*, *4*(1), 13–67.

964   Schmale, J., Zieger, P., & Ekman, A. M. L. (2021). Aerosols in current and future Arctic climate.

965   *Nature Climate Change*, *11*(2), 95–105. doi:10.1038/s41558-020-00969-5

966   Scholz, P., Sidorenko, D., Gurses, O., Danilov, S., Koldunov, N., Wang, Q., et al. (2019).

967   Assessment of the Finite-volumE Sea ice-Ocean Model (FESOM2.0) – Part 1: Description of

968   selected key model elements and comparison to its predecessor version. *Geosci. Model Dev.*,

969   *12*(11), 4875–4899. doi:10.5194/gmd-12-4875-2019

970   Schourup-Kristensen, V., Sidorenko, D., Wolf-Gladrow, D. A., & Völker, C. (2014). A skill

971   assessment of the biogeochemical model REcoM2 coupled to the Finite Element Sea Ice–Ocean

972   Model (FESOM 1.3). *Geoscientific Model Development*, *7*(6), 2769–2802. doi:10.5194/gmd-7-

973   2769-2014

974   Schourup-Kristensen, V., Wekerle, C., Wolf-Gladrow, D. A., & Völker, C. (2018). Arctic Ocean

975   biogeochemistry in the high resolution FESOM 1.4-REcoM2 model. *Progress in Oceanography*,

976   *168*, 65–81. doi:10.1016/j.pocean.2018.09.006

977   Schourup-Kristensen, V., Wekerle, C., Danilov, S., & Völker, C. (2021). Seasonality of

978   Mesoscale Phytoplankton Control in Eastern Fram Strait. *Journal of Geophysical Research:*

979   *Oceans*, *126*(10), e2021JC017279. doi:10.1029/2021JC017279

980   Serreze, M. C., & Barry, R. G. (2014). *The Arctic Climate System* (2nd ed.). Cambridge

981   University Press. doi:10.1017/CBO9781139583817

982   Serreze, M. C., & Meier, W. N. (2019). The Arctic's sea ice cover: trends, variability,

983   predictability, and comparisons to the Antarctic. *Annals of the New York Academy of Sciences*,

984   *1436*(1), 36–53. doi:10.1111/nyas.13856

985   Shupe, M. D., & Intrieri, J. M. (2004). Cloud Radiative Forcing of the Arctic Surface: The

986   Influence of Cloud Properties, Surface Albedo, and Solar Zenith Angle. *Journal of Climate*,

987   *17*(3), 616–628. doi:10.1175/1520-0442(2004)017<0616:CRFOTA>2.0.CO;2

988   Steele, D. J., Franklin, D. J., & Underwood, G. J. C. (2014). Protection of cells from salinity

989   stress by extracellular polymeric substances in diatom biofilms. *Biofouling*, *30*(8), 987–998.

990   doi:10.1080/08927014.2014.960859

991   Steele, M., Morley, R., & Ermold, W. (2001). PHC: A Global Ocean Hydrography with a High-

992   Quality Arctic Ocean. *Journal of Climate*, *14*(9), 2079–2087. doi:10.1175/1520-

993   0442(2001)014<2079:PAGOHW>2.0.CO;2

994   Stroeve, J., & Notz, D. (2018). Changing state of Arctic sea ice across all seasons.

995   *Environmental Research Letters*, *13*(10), 103001.

996   Taylor, P. C., Boeke, R. C., Boisvert, L. N., Feldl, N., Henry, M., Huang, Y., et al. (2022).

997   Process Drivers, Inter-Model Spread, and the Path Forward: A Review of Amplified Arctic

998   Warming. *Frontiers in Earth Science*, *9*. Retrieved from

999   https://www.frontiersin.org/article/10.3389/feart.2021.758361

1000   Terhaar, J., Lauerwald, R., Regnier, P., Gruber, N., & Bopp, L. (2021). Around one third of

1001   current Arctic Ocean primary production sustained by rivers and coastal erosion. *Nature*

1002   *Communications*, *12*(1), 169. doi:10.1038/s41467-020-20470-z

1003   Tsujino, H., Urakawa, S., Nakano, H., Small, R. J., Kim, W. M., Yeager, S. G., et al. (2018).

1004   JRA-55 based surface dataset for driving ocean–sea-ice models (JRA55-do). *Ocean Modelling*,

1005   *130*, 79–139. doi:10.1016/j.ocemod.2018.07.002

1006   Vihma, T., Screen, J., Tjernström, M., Newton, B., Zhang, X., Popova, V., et al. (2016). The

1007   atmospheric role in the Arctic water cycle: A review on processes, past and future changes, and

1008   their impacts. *Journal of Geophysical Research: Biogeosciences*, *121*(3), 586–620.

1009   doi:10.1002/2015JG003132

1010   Wang, Q., Danilov, S., Sidorenko, D., Timmermann, R., Wekerle, C., Wang, X., et al. (2014).

1011   The Finite Element Sea Ice-Ocean Model (FESOM) v.1.4: formulation of an ocean general

1012   circulation model. *Geoscientific Model Development*, *7*(2), 663–693. doi:10.5194/gmd-7-663-

1013   2014

1014   Wang, Q., Wekerle, C., Danilov, S., Wang, X., & Jung, T. (2018). A 4.5 km resolution Arctic

1015   Ocean simulation with the global multi-resolution model FESOM 1.4. *Geoscientific Model*

1016   *Development*, *11*(4), 1229–1255. doi:10.5194/gmd-11-1229-2018

1017   Wang, Qiang, Koldunov, N. V., Danilov, S., Sidorenko, D., Wekerle, C., Scholz, P., et al.

1018   (2020). Eddy Kinetic Energy in the Arctic Ocean From a Global Simulation With a 1-km Arctic.

1019   *Geophysical Research Letters*, *47*(14), e2020GL088550. doi:10.1029/2020GL088550

1020   Wekerle, C., Wang, Q., Danilov, S., Schourup-Kristensen, V., von Appen, W.-J., & Jung, T.

1021   (2017). Atlantic Water in the Nordic Seas: Locally eddy-permitting ocean simulation in a global

1022   setup. *Journal of Geophysical Research: Oceans*, *122*(2), 914–940. doi:10.1002/2016JC012121

1023   Wendisch, M., Macke, A., Ehrlich, A., Lüpkes, C., Mech, M., Chechin, D., et al. (2019). The

1024   Arctic cloud puzzle: Using ACLOUD/PASCAL multiplatform observations to unravel the role

1025   of clouds and aerosol particles in arctic amplification. *Bulletin of the American Meteorological*

1026   *Society*, *100*(5), 841–871.

1027   Wilson, T. W., Ladino, L. A., Alpert, P. A., Breckels, M. N., Brooks, I. M., Browse, J., et al.

1028   (2015). A marine biogenic source of atmospheric ice-nucleating particles. *Nature*, *525*(7568),

1029   234–238. doi:10.1038/nature14986

1030   Wurl, O., Wurl, E., Miller, L., Johnson, K., & Vagle, S. (2011). Formation and global

1031   distribution of sea-surface microlayers. *Biogeosciences*, *8*(1), 121–135. doi:10.5194/bg-8-121-

1032   2011

1033   Wurl, Oliver, & Cunliffe, M. (2017). Transparent exopolymeric particles: an important EPS

1034   component in seawater. *The Perfect Slime: Microbial Extracellular Polymeric Substances (EPS)*,

1035   249.

1036   Yamada, Y., Fukuda, H., Uchimiya, M., Motegi, C., Nishino, S., Kikuchi, T., & Nagata, T.

1037   (2015). Localized accumulation and a shelf-basin gradient of particles in the Chukchi Sea and

1038   Canada Basin, western Arctic. *Journal of Geophysical Research: Oceans*, *120*(7), 4638–4653.

1039   doi:10.1002/2015JC010794

1040   Zamanillo, M., Ortega-Retuerta, E., Nunes, S., Rodríguez-Ros, P., Dall'Osto, M., Estrada, M., et

1041   al. (2019). Main drivers of transparent exopolymer particle distribution across the surface

1042   Atlantic Ocean. *Biogeosciences*, *16*(3), 733–749. doi:10.5194/bg-16-733-2019

1043   Zampieri, L., Kauker, F., Fröhle, J., Sumata, H., Hunke, E. C., & Goessling, H. F. (2021). Impact

1044   of Sea-Ice Model Complexity on the Performance of an Unstructured-Mesh Sea-Ice/Ocean

1045   Model under Different Atmospheric Forcings. *Journal of Advances in Modeling Earth Systems*,

1046   *13*(5), e2020MS002438. doi:10.1029/2020MS002438

1047   Zeising, M., Oziel, L., Gürses, Ö., Hauck, J., Losa, S., Thoms, S., & Bracher, A. (2023).

1048   FESOM2.1-REcoM3 4.5 km model analysis for biogenic aerosol precursors in the Arctic Ocean.

1049   *Zenodo*. Retrieved from https://doi.org/10.5281/zenodo.7886868

1050   Zeppenfeld, S., Bracher, A., Wiegmann, S., Zeising, M., Fuchs, S., Van Pinxteren, M., &

1051   Herrmann, H. (2023). Dissolved and particulate combined carbohydrates, pH, inorganic ions,

1052   CDOM and particulate absorption of SML and bulk water in Arctic surface seawater and melt

1053   ponds. *PANGAEA - Data Publisher for Earth & Environmental Science*. Retrieved from

1054   https://doi.org/xx.xx/PANGAEA.xxxxxx [DOI registration in progess]

1055   Zeppenfeld, S., van Pinxteren, M., Engel, A., & Herrmann, H. (2020). A protocol for quantifying

1056   mono- and polysaccharides in seawater and related saline matrices by electro-dialysis (ED) –

1057   combined with HPAEC-PAD. *Ocean Science*, *16*(4), 817–830. doi:10.5194/os-16-817-2020

1058   Zeppenfeld, Sebastian, van Pinxteren, M., Hartmann, M., Bracher, A., Stratmann, F., &

1059   Herrmann, H. (2019). Glucose as a Potential Chemical Marker for Ice Nucleating Activity in

1060   Arctic Seawater and Melt Pond Samples. *Environmental Science & Technology*, *53*(15), 8747–

1061   8756. doi:10.1021/acs.est.9b01469